Antimicrobial Activity of Rhenium Di- and Tricarbonyl Diimine Complexes: Insights on Membrane-Bound *S. aureus* Proteins Binding

Kevin Schindler [1,†], Youri Cortat [1,†], Miroslava Nedyalkova [1], Aurélien Crochet [1], Marco Lattuada [1], Aleksandar Pavic [2,*] and Fabio Zobi [1,*]

[1] Department of Chemistry, Fribourg University, Chemin Du Musée 9, 1700 Fribourg, Switzerland
[2] Institute of Molecular Genetics and Genetic Engineering, University of Belgrade, Vojvode Stepe 444a, 11042 Belgrade, Serbia
* Correspondence: fabio.zobi@unifr.ch; sasapavic@imgge.bg.ac.rs
† These authors contributed equally to this paper

Abstract: Antimicrobial resistance is one of the major human health threats with significant impact on the global economy. Antibiotics are becoming increasingly ineffective as drug-resistance spreads, imposing an urgent need for new and innovative antimicrobial agents. Metal complexes are an untapped source of antimicrobial potential. Rhenium complexes, amongst others, are particularly attractive due to their low *in vivo* toxicity and high antimicrobial activity, but little is known about their targets and mechanism of action. In this study, a series of rhenium di- and tricarbonyl diimine complexes was prepared and evaluated for their antimicrobial potential against 8 different microorganisms comprising Gram-negative and -positive bacteria. Our data showed that none of the Re dicarbonyl or neutral tricarbonyl species have either bactericidal or bacteriostatic potential. In order to identify possible targets of the molecules, and thus possibly understand the observed differences in the antimicrobial efficacy of the molecules, we computationally evaluated the binding affinity of active and inactive complexes against structurally characterized membrane bound *S. aureus* proteins. The computational analysis indicates two possible major targets for this class of compounds, namely lipoteichoic acids flippase (LtaA) and lipoprotein signal peptidase II (LspA). Our results, consistent with published *in vitro* studies, will be useful for future design of rhenium tricarbonyl diimine-based antibiotics.

Keywords: rhenium; tricarbonyl; antimicrobial, S. aureus, MRSA, AutoDock, membrane, proteins, LspA, LtaA.

1. Introduction

The expansion of resistance to conventional antibiotics has become a notable health threat, and imposed the development of alternative treatment options for battling such a global problem [1]. Amongst the six nosocomial pathogens that exhibit multidrug resistance and virulence, methicillin-resistant *S. aureus* (MRSA) is a major cause of community and hospital acquired infections worldwide, ranging from superficial skin and soft tissue infections [2] to invasive infections and sepsis [3]. This pathogen represents the most common and the second most common cause of healthcare-associated and bloodstream infections (BSI), as well as the most important cause of BSI death [4]. Since the bacterium is increasingly showing resistance to multiple antibiotics, the World Health Organization listed it in 2017 into the high priority group of human pathogens. Indeed, the same year, the Centers for Disease Control and Prevention (CDC), reported that more than 119,000 people suffered from *S. aureus* bloodstream infections in the United States, with nearly 20,000 of them (> 16%) eventually dying.

What has exacerbated the problem of antimicrobial resistance (AMR) is the fact that fewer new antibiotics are reaching the market, with the last entirely original class of antibiotic discovered in the late 1980s. This is because large pharmaceutical companies have left the market due to lack of financial incentive [5]. Consequently, in the last few years, academic research groups at universities around the globe have taken the challenge to prepare and discover new antibiotic drugs that may serve as lead compounds for new structurally viable drugs. In our era, strategies for the discovery and development of new drugs combine computational and experimental approaches. This is true in virtually all medicinal discovery areas including design and discovery of molecules as proper candidates for treatment of *Staphylococcus aureus* infection. Computer-aided drug design (CADD) methods are computational approaches to guide and expedite the experimental findings for new drug design processes [6-10]. CADD can be used in a qualitative and quantitative mode, to improve the biovalidity and prediction rates for ligand binding affinity, and specificity in a manner that can lead to identification of biological targets of known drugs and the design process of new agents in an easier, more efficient and less expensive manner. In a fashionable drug design process, typically hundreds of compounds can be tested in a short time. The existing methodologies as e.g. site-identification by ligand competitive saturation (SILCS) [8,11] have become a versatile tool in ligand-protein binding prediction. The foundation of CADD technique is based on molecular docking [12-14] and molecular dynamics simulations [15,16].

Within the specific context of this article, CADD has been used e.g. to evaluate medicinal plants-derived active compounds that could be used as therapeutic alternatives for MRSA infection [17-20]. The study of receptor-ligand interaction in the frame of molecular docking has increased the importance of probing the efficiency of these plant-derived antimicrobial agents [17,18] and testing antimicrobial activity using screened lead compounds focusing on the role of computational screening methods [20-23] in tackling the problem. However, a major strategy still pursued in the field is that of modifying already approved antibiotics [24]. As it may be expected, all of these molecules are purely organic compounds. While some of these new derivatives (some currently in preclinical or clinical development) will provide feasible short-term solutions, it is probable that the pathogens will rapidly adapt and develop resistance to these molecules as well [24].

As an alternative to organic compounds, there is an increasing awareness in academia of the potential of metal complexes to act as the new class of molecules for the purpose. Indeed, the unique chemistry and larger variety of 3D geometries of metal compounds can address targets and modes of action unavailable to organic molecules. In the last decade, complexes of virtually all transition metals have been evaluated as antimicrobial agents [25-28], with rhenium (Re), among others [29,30], showing promising potential for new antibiotic development [31-34]. While some transition metal complexes [35-40], predominantly of group 8 [41-43] and 9 [44-47], act against Gram-negative bacteria, carbonyl rhenium complexes have demonstrated very potent activity towards Gram-positive pathogens, particularly towards *Staphylococcus aureus* involving both methicillin-resistant (MRSA) and methicillin-sensitive (MSSA) strains [32-34,48-50].

Our group has been principally interested in the development of the chemistry of carbonyl rhenium complexes [51-53] for their use in different medicinal applications [54-59], including their evaluation as anticancer [60-63] and antibacterial agents [49,50]. Due to their very low *in vivo* toxicity [64-67], tricarbonyl complexes of rhenium are particularly attractive. The same type of molecules (i.e. those of the *fac*-$[Re(CO)_3]^+$ core) are also the ones most widely investigated, showing the highest anticancer and antimicrobial effectiveness against *S. aureus* strains. It is still unclear what molecular features of carbonyl rhenium complexes make them such promising medicinal agents. In a study that we have recently reported [49], we concluded that, unlike anticancer complexes, positively charged rhenium species are most effective against the microbes, and we hypothesized that charged compounds may more strongly interact with phosphatidylglycerol and cardiolipin anionic membrane lipids. Later, however, we found that by substitution of a single

neutral carbonyl ligand for a nitrosonium cation, the compounds lose their antimicrobial effect [52]. Thus, in terms of their antibacterial effectiveness, both the required molecular features and mechanism of action of these agents remain largely unknown.

In order to advance knowledge on the issues just mentioned above, we evaluated the antimicrobial activity of dicarbonyl rhenium diimine complexes (i.e. of the *cis*-$[Re(CO)_2]^{+/2+}$ core) and compared the same to those of structurally similar *fac*-$[Re(CO)_3]^+$ species. This part of study was performed because: a) no antimicrobial data is available on carbonyl complexes of the *cis*-$[Re(CO)_2]^{+/2+}$ core lacking other π-acid ligands; and b) a comparison of the activity of *cis*-$[Re(CO)_2]^{+/2+}$ and structurally similar *fac*-$[Re(CO)_3]^+$ species may provide information about the key molecular features required for design of an effective Re-based antibiotic agent. Furthermore, we computationally evaluated the binding affinity of all compounds (both active and inactive molecules) against structurally characterized membrane bound *S. aureus* proteins. We performed this study principally to: a) identify possible biological targets of active complexes; b) possibly understand the underlying reasons for the observed differences in the antimicrobial efficacy of Re complexes; and c) offer a support for rational design of rhenium complexes based on the computational protocol for computer-aided drug design (CADD).

2. Results and Discussion

2.1. Synthesis and Characterization of Metal Complexes

Rhenium carbonyl complexes investigated in this study were prepared according to the procedures illustrated in scheme 1. Tricarbonyl species **6**-**10** (Figure 1) were obtained in high yield and purity according to established routes generally used in the preparation of these compounds. *fac*-$[Re(CO)_3(NN)Br]$ complexes (**6**-**8**, **9a** and **10**, where NN = relevant bidentate diimine ligand) may be obtained in one step from $[Re(CO)_5Br]$ by boiling this precursor in toluene in the presence of one equivalent of NN. The resulting yellow product, isolated by filtration, is generally of high purity (> 96% by NMR or HPLC) and can be used for further modification by substitution reaction of the coordinated bromide atom by other monodentate ligands as for species **9b** and **9c**. For this reaction we found that the best conditions consist in the treatment of a *fac*-$[Re(CO)_3(NN)Br]$ complex with trifluoromethanesulfonic acid to produce the intermediate *fac*-$[Re(CO)_3(NN)(CF_3SO_3)]$ molecule, followed by addition of L (where L = pyridine: py or *N*-methyl imidazole: MeIm). The reaction is also high yielding, but the desired *fac*-$[Re(CO)_3(NN)L]CF_3SO_3$ salt requires purification on alumina or via HPLC.

The preparation of dicarbonyl *cis*-$[Re(CO)_2(NN)X_2]$ species (**1**-**5** and **11**, where X = Br or L, Figure 1) is more demanding and requires several steps from the common $[Re(CO)_5Br]$ precursor. We have recently published the details of this chemistry [51], showing that the synthetic route is favorable if X is a halide or an aromatic heterocycle (or a combination of both). However, yields of *cis*-$[Re(CO)_2(NN)X_2]$ species are much lower than comparable *fac*-$[Re(CO)_3(NN)Br]$ complexes. Briefly, *cis*-$[Re(CO)_2(NN)X_2]$ species may be prepared following the sequential two electron oxidation of *fac*-$[Re(CO)_3Br_3]^{2-}$ to *cis*-$[Re(CO)_2Br_4]^-$ [68], the one electron reduction to *cis*-$[Re(CO)_2Br_4]^{2-}$, complexation of NN to *cis*-$[Re(CO)_2(NN)Br_2]$, one electron reduction to *cis*-$[Re(CO)_2(NN)Br_2]^-$, and, finally, the stepwise substitution of Br by L to *cis*-$[Re(CO)_2(NN)BrL_2]$ and *cis*-$[Re(CO)_2(NN)L_2]^+$. It is interesting to point out here, that, contrary to other similar complexes, the presence of NN in the coordination sphere of the 17-electron Re^{II} complexes (**1a**-**c** and **11**) imparts stability to the molecules which are stable in solution and do not decompose by releasing CO [69,70].

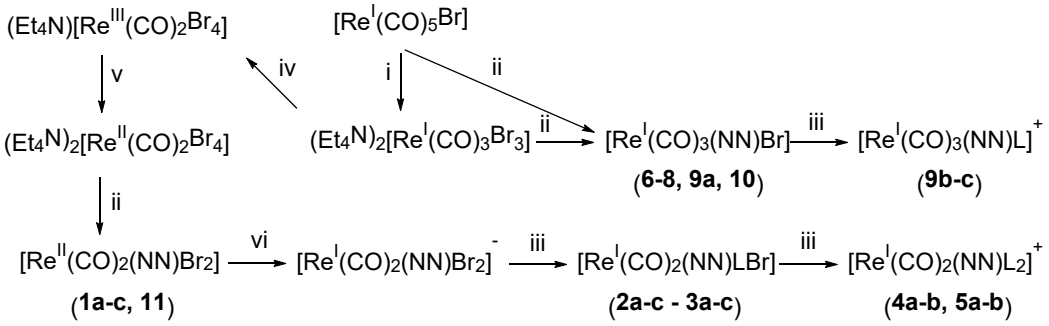

Scheme 1. Synthetic scheme for the preparation of the complexes investigated in this study. NN = relevant bidentate diamine ligand; L = pyridine (py) or *N*-methyl imidazole (MeIm). General conditions: i: Et_4NBr, diglyme; ii: NN, ethanol/water, toluene or CH_2Cl_2; iii: L, methanol or neat L; iv: Br_2, CH_2Cl_2; v: tetrakis(dimethylamino)ethylene, acetonitrile, under N_2; vi: tetrakis(dimethylamino)ethylene, CH_2Cl_2, under N_2. For more details, refer to section 4.

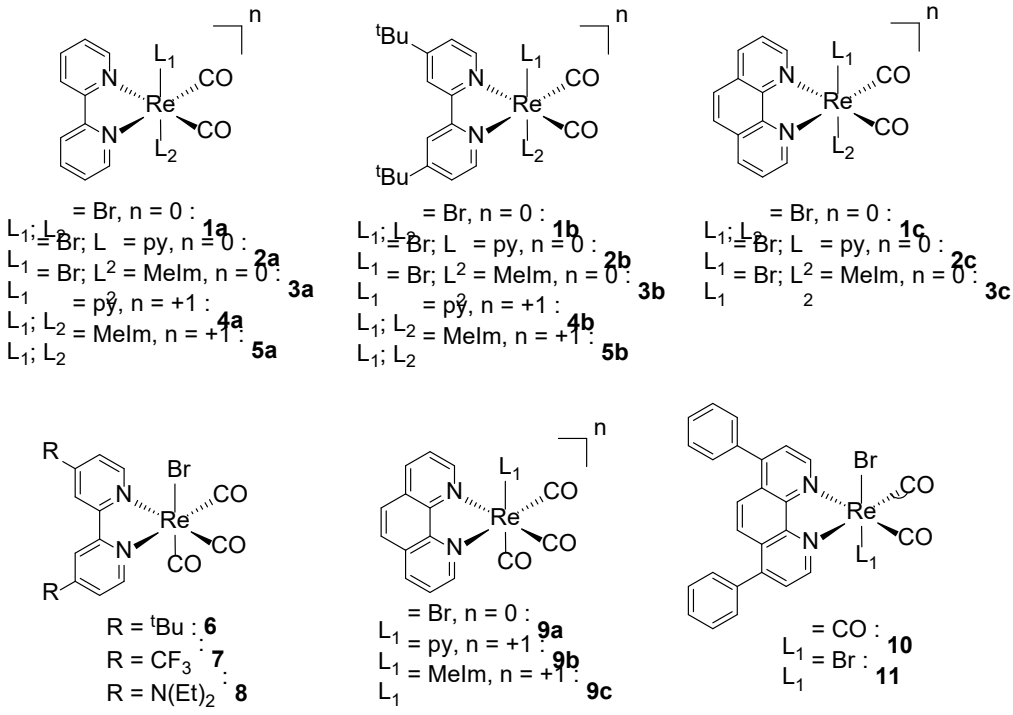

Figure 1. Structures and codes of tested Re dicarbonyl (**1-5**) and tricarbonyl (**6-10**) complexes.

New complexes were characterized by standard techniques, including X-ray crystallography for dicarbonyl species **4a** and **11** (Figure 2) and trycarbonyl complexes **6**-**8** and **10** (Figure 3). Within the series of dicarbonyl *cis*-$[Re(CO)_2(NN)Br_2]$ species, the preparation of compound **11** (where NN = bathophenanthroline: batho-phen) was particularly challenging. Indeed, the reaction of either *cis*-$[Re^{III}(CO)_2Br_4]^-$ or *cis*-$[Re^{II}(CO)_2Br_4]^{2-}$ with bathophen leads to a mixture of products which are very difficult to separate. Normally, *cis*-$[Re(CO)_2(NN)Br_2]$ complexes are obtained as *cis-cis-trans* species (with the two Br atoms in *trans* position to each other). Only when one of the bromides is substituted for L, the intermediate penta-coordinated complexes undergo Berry pseudorotation which establishes an equilibrium between the *cis-cis-trans* and *cis-cis-cis* isomers [51]. These can be separated by column chromatography and crystallized separately (as it is the case of **3a**,

Figure 2). In the preparation of **11**, we found, not only that the reaction leads to disproportionation giving **10**, but also that the *cis-cis-cis* isomer of **11** (*cis*-**11**) and the mono carbonyl *mer*-[Re(CO)(NN)Br_3] complex (*mer*-**12**, Figure 2) are formed. Complex **11** can be separated from the mixture, but despite our efforts, the other complexes formed could not be eluted separately in our chromatographic purification procedures. We should underline here that we were able to identify the products obtained in the reaction only by co-crystallizing them from a mixture. We also note that, to our knowledge, *mer*-[Re(CO)(NN)Br_3] (*mer*-**12**) is a unique example of a diimine rhenium mono carbonyl complex structurally characterized.

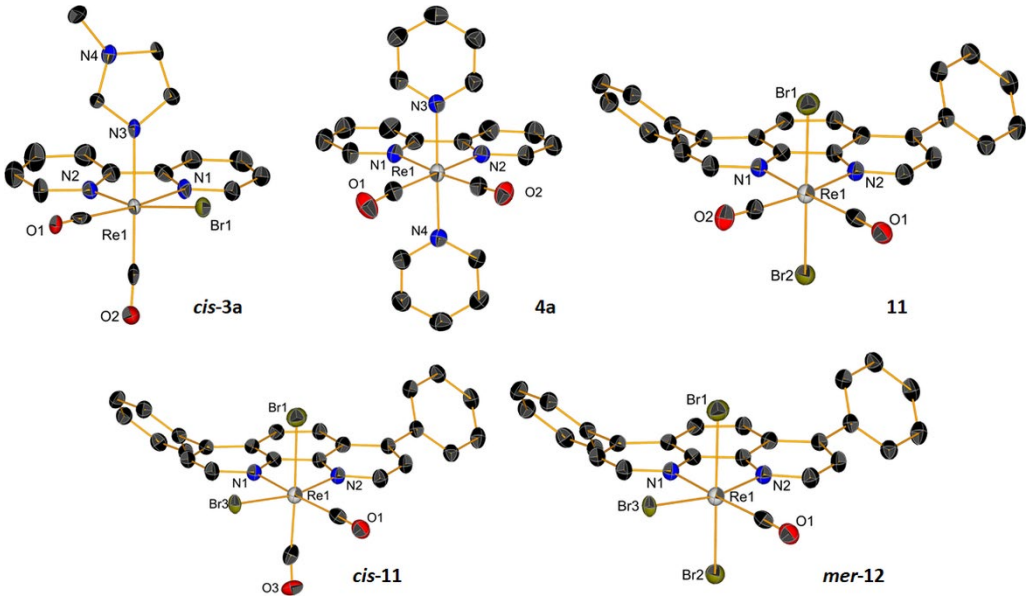

Figure 2. ORTEP representations of crystal structures of Re dicarbonyl complexes. Thermal ellipsoids are at 30% probability. Hydrogen atoms are omitted for clarity. **Note**: Compounds *cis*-**11** and *mer*-**12** co-crystallize in a mixture where **10** and **11** are also present.

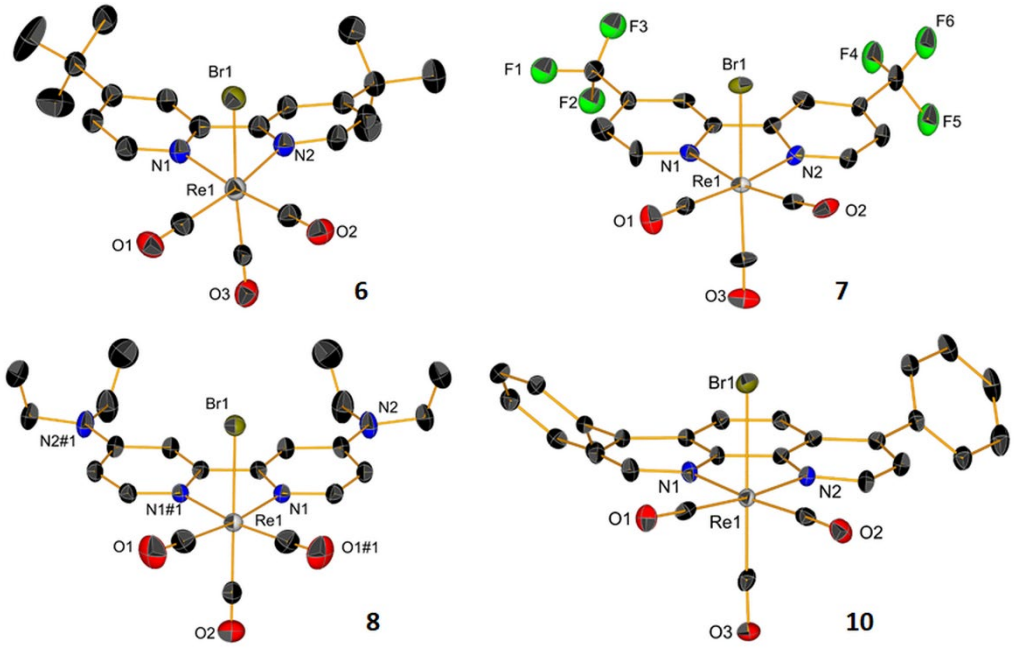

Figure 3. ORTEP representations of crystal structures of Re tricarbonyl complexes **6-8** and **10**. Thermal ellipsoids are at 30% probability. Hydrogen atoms are omitted for clarity.

2.2. Antimicrobial Properties of Complexes

The antimicrobial activity of complexes **1**-**11** (15 neutral, 6 cationic) was determined against 8 different microorganisms including four Gram-negative bacteria (*Enterobacter cloaceae* ATCC 3047, *Klebsiella pneumoniae* ATCC 13803, *Acinetobacter baumanii* ATCC 19606, *Pseudomonas aeruginosa* PAO1 NCTC10332), two Gram-positive bacteria (methicillin-resistant *Staphylococcus aureus* MRSA43300 and methicillin-sensitive *S. aureus* ATCC25923) and two fungi (*Candida albicans* SC5314 and *C. auris*, a clinical strain). The species of these two genera are responsible for the majority of hospital-acquired infections and are challenging to treat, especially their co-infections [71]. The results of our study are given in Table 1. We found that none of the dicarbonyl complexes showed antimicrobial potential. Only compounds **4b**, **5b** and **11** were weakly active against *S. aureus* strains, but their MIC values (25 and 50 μM, respectively) are much higher than active rhenium complexes **13**-**19** (Figure 4) [32,33,48-50].

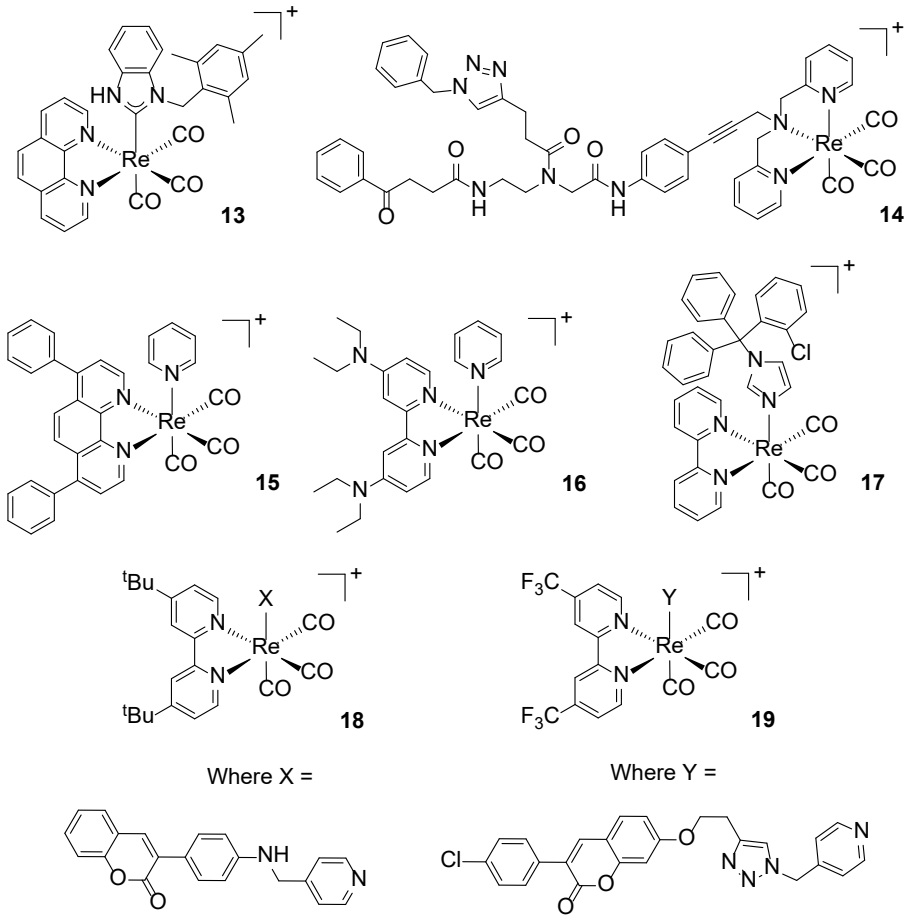

Figure 4. Structures of previously published active *fac*-$[Re(CO)_3]^+$ complexes. Complex **13** [33]; complex **14** [32]; complexes **15**, **16**, **18** and **19** [49,50]; complex **17** [48].

Table 1. Antimicrobial activity addressed by determining the minimal inhibitory concentration (MIC, μM) of different Re-bearing complexes.

Compound	*A. baumanii*	*P. auruginosa*	*K. pneu-moniae*	*S. aureus* MRSA	*S. aureus* MSSA	*E. cloaceae*	*C. albicans*	*C. auris*
1a-5a	>100	>100	>100	>100	>100	>100	>100	>100
1b-3b	>100	>100	>100	>100	>100	>100	>100	>100
4b	>100	>100	>100	25	25	>100	>100	>100
5b	>100	>100	>100	50	50	>100	>100	>100
1c-3c	>100	>100	>100	>100	>100	>100	>100	>100
6-8, 9a-c, 10	>50	>50	>50	>50	>50	>50	>50	>50
11	>100	>100	>100	50	50	>100	>100	>100
13	n.d.	n.d.	n.d.	0.7	22.8	n.d.	n.d.	n.d.
14	n.d.	n.d.	n.d.	1.6	1.6	n.d.	n.d.	n.d.
15	n.d.	n.d.	n.d.	0.4	0.6	n.d.	6.2	50
16	n.d.	n.d.	n.d.	0.8	0.8	n.d.	6.2	n.d.
17	8	32	32	0.25	0.25	n.d.	n.d.	n.d.
18	n.d.	n.d.	n.d.	0.8	3.1	n.d.	3.1	n.d.
19	n.d.	n.d.	n.d.	1.6	6.2	n.d.	n.d.	n.d.

n.d. = not determined

2.3. Molecular docking study - membrane bound S. aureus proteins

The results obtained from our *in vitro* antimicrobial investigation prompted a fundamental question, namely: "what sets apart cationic *fac*-$[Re(CO)_3]^+$ complexes from other structurally similar neutral complexes or compounds lacking the tricarbonyl core?". Or, in other words, "why are complexes **13**-**19** (Figure 4) active antimicrobial agents while other rhenium complexes are not?" Compounds **13**-**19** are different molecules, but they share some common features (e.g. same charge, a lipophilic diimine or polydentate ligand with a pyridine in the coordination sphere). In addition, Table 2 presents the predictability rate of the drug-likeness properties for these rhenium complexes. The descriptor values were retrived from the AlvaDesc v.2 software (Milano, Italy) [72].

Table 2. Drug likeness properties of active antimicrobial rhenium complexes **13**-**19**.

Compound	MW	RBN	TPSA(Tot)	HBA	HBD	LOGP99	BLTF96	BLTA96	BLTD48	ESOL	cRo5	Ro5
13	700.827	3	81.79	6	1	6.8	-3.09	-3.22	-3.23	-7.19	1	0
14	1072.267	16	187.36	14	2	4.8	1.13	1.49	1.73	-5.67	0	1
15	681.767	3	66	0	6	6.7	-2.99	-3.11	-3.11	-7.02	1	0
16	647.827	7	72.48	0	8	4.1	-2.03	-2.04	-1.98	-4.94	1	0
17	771.297	5	70.93	8	0	7.1	-3.94	-4.17	-4.23	-7.85	1	0
18	867.067	3	108.24	2	1	8.5	-4.13	-4.38	-4.45	-8.74	1	0
19	1021.367	8	136.15	0	12	8.0	-3.84	-4.06	-4.11	-9.29	0	1

Labels: MW - molecular weight, RBN - rotatable bond number, TPSA - total polar surface area in A^2, HBA—number of H bond acceptors, HBD—number of H bond donors, LOGP99 - Wildmann-Crippen octanol-water partition coeff., BLTF96 - Verhaar Fish base-line toxicity from MLOGP (mmol/l), BLTD48 - Verhaar Daphnia base-line toxicity from MLOGP (mmol/l), BLTA96 - Verhaar Algae base-line toxicity from MLOGP (mmol/l), ESOL—estimated solubility (logS) for aqueous solubility using LOGPcons., cRo5 - Complementary Lipinski Alert index, Ro5 – Lipinski Rule of 5

At this early stage of investigation, to aid finding an answer to the question, a pure experimental approach focused on e.g. microbial gene expression analysis and transcriptomic data, would be costly and time consuming. We thus decided to adopt an *in silico* approach in order to guide future synthetic, SAR and mechanistic studies. There are fortunately some experimental facts that helped us focus our attention on specific enzyme that may be considered as possible targets for one or more of compounds **13**-**19**. Although mechanistic studies are limited and specific biological targets still unknown, effective antimicrobial *fac*-$[Re(CO)_3]^+$ complexes appear to act predominately on the membrane of the bacteria. The complex of Metzler-Nolte and Bandow, i.e. compound **14** in Figure 4, targets the cytoplasmic membrane of *Bacillus subtilis*, affecting its architecture and disrupting essential cellular processes taking place at the membrane, such as respiration, and cell wall biosynthesis and integrity [31]. Similarly Mendes *et al.* have shown that the mechanism of action of the *fac*-$[Re(CO)_3(bpy)(ctz)]^+$ complex (**17** in Figure 4, where ctz = the drug clotrimazole) involves a sequence of events initiated by membrane insertion, followed by membrane disorganization, inhibition of peptidoglycan biosynthesis, and break down of the membrane potential [48].

Based on these data, and in order to possibly understand the differences in the antimicrobial effects of previously published active *fac*-$[Re(CO)_3]^+$ complexes (**13**- **19**, Figure 4) and inactive *fac*-$[Re(CO)_3]^+$ and *cis*-$[Re(CO)_2]^n$ complexes, we decided to investigate the binding affinity of all above compounds against membrane bound *S. aureus* proteins. The *in silico* docking studies were also performed in order to gain insights about possible targets of the molecules by careful analysis of the data. A PDB search revealed that nine structurally characterized membrane bound *S. aureus* MRSA proteins are available on the database. Of these we selected eight, comprising four penicillin-binding proteins (PBPs) [73-76] and the following enzymes: lipoteichoic acids synthase [77] (specifically its extracellular catalytic domain, eLtaS), type-I signal peptidase (SpsB) [78], lipoprotein signal peptidase II (LspA) [79], and lipoteichoic acids flippase (LtaA) [80]. Pre-screening of binding affinities (*b.a.*) was performed with the AutoDock Vina software [14]. Calculated *b.a.* were recorded as docking scores in kilocalories per mole (kcal/mol) and the results are given in Supplementary Materials (Tables S1a and S1b). In the initial screening, metal complexes were first docked at the known inhibitor-binding site of the specific protein and the *b.a.* compared to that of the same inhibitor. At this stage, only proteins where complexes showed *b.a.* of ca. -9.0 kcal/mol and greater than the corresponding inhibitor *b.a.* (Δ values in Tables S1a and S1b), or *b.a.* of ca. -10.0 kcal/mol and comparable to the corresponding inhibitors' *b.a.*, were considered as possible targets for the complexes.

Within the above constrains, and in general terms, our initial analysis revealed the following (detailed values are in Supplementary Materials, Tables S1a and S1b).

1) With the exception of the *cis*-$[Re(CO)_2]^n$ complexes **1b**-**3b** and the *fac*-$[Re(CO)_3]^+$ complexes **6**, **7** and **10**, none of the inactive rhenium di- or tricarbonyl compounds showed any *b.a.* for the enzyme evaluated.

2) Inactive molecules **1b**-**3b**, **6**, **7** and **10** showed affinity for the penicillin-binding protein 4 (PBP4) with *b.a.* ranging from -8.9 (**1b**) to -12.3 (**10**) kcal/mol.

3) Compound **10** also showed good affinity for lipoteichoic acids flippase (LtaA) with *b.a.* of -10.3 kcal/mol.

4) Amongst active antimicrobial rhenium complexes (i.e. molecules **13**-**19**, Figure 4), complexes **16** and **17** showed the lowest *b.a.* for the selected enzymes. These were higher than inactive compounds but lower than known inhibitors.

5) With variations within the series, other active antimicrobial rhenium complexes (**13**-**15** and **18**-**19**) showed good *b.a.* for five enzymes. These are: the penicillin-binding protein 4 (PBP4, *b.a.* ranging from -9.1 (**13**) to -10.7 (**19**) kcal/mol). Type-I signal peptidase (SpsB, all complexes except **14**, *b.a.* ranging from -9.1 (**13**) to -10.4 (**19**) kcal/mol). Lipoteichoic acids synthase (LtaS, only **15**, **18** and **19**, *b.a.* ranging from -9.4 (**15**) to -10.9 (**19**) kcal/mol). Lipoteichoic acids flippase (LtaA, only **15**, **18** and **19**, *b.a.* ranging from -10.4 (**15**)

to -11.3 (**19**) kcal/mol). Lipoprotein signal peptidase II (LspA, all complexes except **13**, *b.a.* ranging from -8.7 (**15**) to -10.6 (**18**) kcal/mol).

Interestingly, PBP4, LtaS and LtaA are all involved in bacterial wall biosynthesis [76,78,80-84]. PBP4 is a transpeptidase that performs the crosslinking reaction in the synthesis of the peptidoglycan backbone [84]. LtaS catalyzes the polymerization of lipoteichoic acid (LTA) polyglycerol phosphate, a reaction that presumably uses phosphatidylglycerol as substrate [77]. The enzyme is required for staphylococcal growth and cell division process [85,86]. LtaA acts upstream of LtaS [87], and it is presumed to catalyse the translocation reaction of anchor lipid-linked-disaccharide gentiobiosyl-diacylglycerol from cytoplasmic leaflet of the membrane to the extracellular side of the plasma membrane where lipoteichoic acids are assembled [80-83]. A flippase with similar structure (MurJ) [88,89], is also involved in the translocation of disaccharide-pentapeptide building blocks attached to a polyisoprene lipid carrier (called lipid II) across the cytoplasmic membrane where peptidoglycan polymerization (i.e. the polysaccharide matrix that protects bacteria from osmotic lysis) takes place [90]. The remaining two proteins are SpsB and LspA. SpsB is a proteolytic enzyme that plays a crucial role in bacterial viability by processing proteins that are translocated across the membrane [78,91], while LspA is involved in bacterial lipoprotein posttranslational processing [92] and it is essential for the survival and virulence in Gram-positive bacteria [93,94]. This latter enzyme is considered as one of the major targets for the development of new antibiotics [95]. The calculated binding affinities of active Re complexes with these possible targets (*b.a.* ranging from ca. -9 to -11 kcal/mol) are fully consistent with the experimental results reported by Wenzel *et al.*[31] and Mendes *et al.* [48], in that inhibition of these proteins would lead to membrane disorganization and affect peptidoglycan/wall biosynthesis [76,80-84].

Following this initial screening, active complexes **13**-**19** were more comprehensively analysed for their binding towards the selected receptors. Extensive semi-flexible docking was performed, introducing flexibility of the receptors' binding pockets amino acids' side chains and complexes' rotatable bonds. The number of modes was set to 200, and the exhaustiveness was set to 40. Each docked complex was calculated in triplicate mode. The triplication test detects if there is a variation in the obtained clusters compactness of the poses and changes of top-ranked compounds from the previous run, thus one avoids bias in the scoring. If bias in the scoring is present, the solution for such a case, along with the control experiment, was a reduction in the chemical space search (e.g., reduction of search box). The performed protocol provides information as to whether the selected best molecules remain amongst the highest scored compounds of the rank-ordered docking list. After the calibration procedure for the docking, the molecules were virtually screened against the eight-target proteins. The localization of the active pocket amino acid residues was predicted according to Jendele et al. [96]. Results are summarized in Table 3, while detailed ranking of the obtained pockets are in Supplementary Materials (Table S2).

Accordingly, the computational results of this library of compounds are shown in Table 4. For the PBP receptors, the docking protocol identified **15** and **19** as having the greatest *b.a.* for these enzymes, particularly for PBP2a and PBP4 (Table 4). As other non-active rhenium complexes showed *b.a.* for PBP4, we posit that this protein is not a probable target for active complexes. Conversely, the *b.a.* of **15** and **19** for PBP2a is of interest (*b.a.* of -9.2 and -9.8 kcal/mol respectively, Table 4). Expression of penicillin-binding protein 2a (PBP2a) is responsible in methicillin-resistant *S. aureus* (MRSA) for the high-level resistance of the bacteria to β-lactam antibiotics [84]. PBP2a is a unique transpeptidase, as it is capable of catalyzing cell-wall crosslinking despite β-lactam antibiotics. Inhibition of PBP2a by **15** and **19** may thus possibly additionally account for the strong antimicrobial activity of these complexes against MRSA [49,50]. Computationally, in the case of **19**, the stabilization of the protein-drug complex is based on the detected H-bonds between the compound and the surrounding amino acid environment (Ser, Thr and Gln residues). A detailed distribution for the amino acids for the best complexes is given in Supplementary

Materials (Table S3). In this case, the intramolecular backbone H-bonds stabilize the β-turn structure with the ligand position.

Table 3. Predicted binding sites

PBD ID	Area (Å²)	Volume (Å³)	Pocket Residues ID / Flexible chains
2OLV (PBP2)	3500.5	7715.2	ALA_112, VAL_367, GLY_339, LYS_127, LYS_135, THR_150, VAL_153, THR_148, GLU_171, LYS_194, PRO_231, ASN_193, GLY_229
4DKI (PBP2a)	5537.8	9122.9	THR_398, PRO_401, VAL_443, THR_444, SER_461, TYR_519, GLY_520, THR_582, ALA_601, ARG_612, ASP_638
3VSL (PBP3)	9921.9	13845.0	GLY_424, VAL_390, LEU_425, THR_426, MET_453, LEU_518, ASP_519, LYS_618, TYR_636
5TXI (PBP4)	4258.4	4521.5	SER_75, ALA_74, THR_77, LYS_78, SER_137, SER_185, SER_262, PHE_241, THR_260, GLY_261, PRO_113, LEU_115, GLU_114
2W5Q (LtaS)	132.1	103.4	LEU_254, GLU_255, GLN_297, GLY_298, LYS_299, THR_300, SER_301, HIS_347, PHE_353, TRP_354, ASN_355, LYS_397, HIS_416
4WVJ (SpsB)	1922.1	3375.8	TRP_236, GLU_117, GLU_159, TYR_161, ASN_18, ASP_20, LYS_21, LEU_268, SER_343, TRP_346, TYR_347, ARG_350, LYS_48
6S7V (LtaA)	1758.2	2257.5	LEU_219, PRO_221, LEU_225, ALA_229, ILE_230, ALA_230, VAL_234
6RYP (LspA)	8452.7	1485.4	ALA_103, _367, GLY_339, LYS_127, LYS_135, THR_150, VAL_153, THR_148, GLU_171, LYS_194, PRO_231, ASN_193, GLY_229

For the second group of receptors (namely LtaS, SpsB, LtaA and LspA) the docking protocol identified complexes **14**, **15**, **18** and **19** as having high *b.a.* for lipoteichoic acids flippase (LtaA, all complexes except **14**) and lipoprotein signal peptidase II (LspA, see Table 4). As mentioned above, flippases like LtaA catalyse the translocation reactions of anchor lipid-linked-disaccharide gentiobiosyl-diacylglycerol and lipid II across the cytoplasmic membrane where essential cell wall polymers (i.e. lipoteichoic acid and peptidoglycan) are assembled (Figure 5) [80-83,87-90]. LspA, on the other hand, is involved in bacterial lipoprotein posttranslational processing [92] and it is essential for the survival and virulence in Gram-positive bacteria (Figure 6) [93,94]. Possible inhibition of these enzymes by active antibiotic rhenium complexes would disrupts essential cellular processes taking place at the membrane, and ultimately lead to cell death. It should be mentioned that our computational analysis did not identify possible targets for complexes **13**, **16** and **17**. If for the former complexes this indicates that the compounds may exert their antibiotic activity against MRSA via mechanisms not involving membrane-bound proteins, for **17** the results appear to support the experimental evidence of Mendes et al. [31]. Indeed, the authors reported that **17** interferes with the cycling of the undecaprenylprecursor in peptidoglycan biosynthesis ("lipid II cycle"), leading to accumulation of UDP-MurNAc-pentapeptide (i.e. lipid I, the ultimate cytoplasmic peptidoglycan precursor) in the cytoplasm of treated cells. Thus, **17** inhibits the MurG-mediated conversion of lipid I to lipid II [31]. The X-ray structure of MRSA MurG is not available in the PDB database, thus we could not confirm computationally the experimental data of Mendes et al. [31].

Table 4. Molecular docking scores and related properties.

Receptor	Drug	Affinity	H-bonds	Receptor's Rgyr (nm)	System's Rgyr (nm)	Receptor's SASA (nm²)	Receptor's prob. drugability	Ligand's SASA (nm²)	System's SASA (nm²)	Contact Area (nm²)	Detected H-bonds with AA residue
2OLV (PBP2)	**13**	-6.9	3	3.29	3.29	295.26	0.82	7.60	295.24	3.80	ASP 156, LYS 194, PRO 231
	14	-7.4	3	3.29	3.29	295.26	0.82	12.14	294.91	6.24	ASP 156, LYS 194, PRO 231
	15	-8.1	2	3.29	3.28	295.26	0.82	7.87	294.87	4.13	ASP 89
	16	-5.7	4	3.29	3.28	295.26	0.82	8.05	295.15	4.08	THR 87, GLN 92, HIS 94, GLU 95
	17	-7.8	1	3.29	3.32	295.26	0.82	7.90	299.57	3.13	ASP 156
	18	-7.9	1	3.29	3.29	295.26	0.82	10.77	295.17	5.43	PRO 72
	19	-7.2	1	3.29	3.30	295.26	0.82	9.35	295.14	4.73	ASN 237
4DKI (PBP2a)	**13**	-6.7	1	3.66	3.66	317.73	0.76	7.09	316.08	4.10	THR 398
	14	-7.2	3	3.66	3.65	317.73	0.76	11.21	316.08	6.43	THR 398, GLY 520
	15	-9.2	1	3.66	3.66	317.73	0.76	7.55	315.86	4.71	LYS 394
	16	-5.9	4	3.66	3.66	317.73	0.76	7.87	316.27	4.66	THR 600, LEU 603, MER 605
	17	-6.7	4	3.66	3.67	317.73	0.76	7.7	317.2	3.9	ASP 516, GLN 521, MET
	18	-8.5	1	3.66	3.66	317.73	0.76	10.75	316.08	6.94	SER 400
	19	-9.8	4	3.66	3.67	317.73	0.76	11.57	315.25	7.02	SER 403, GLN 521, THR 600, SER 400

3VSL				3.11	3.11		0.81				TYR 525, GLU 623,
(PBP3)	**13**	-7.0	3			301.97		7.25	300.48	4.37	GLN 626
	14	-7.0	3	3.11	3.11	301.97	0.81	12.00	299.12	7.42	
				3.11	3.11		0.81				TYR 525, ASP 519,
	15	-8.6	3			301.97		7.80	300.81	4.48	GLU 623
				3.11	3.11		0.81				
	16	-5.3	1			301.97		8.01	301.13	4.42	GLN 626
	17	-6.9	0	3.11	3.11	301.97	0.81	7.69	300.78	4.44	-
	18	-7.6	2	3.11	3.11	301.97	0.81	11.22	302.30	5.44	GLU 623
	19	-6.7	3	3.11	3.11	301.97	0.81	11.88	301.39	6.23	GLU 623
5TXI				2.16		151.84	0.8				
(PBP4)	**13**	-6.3	0		2.17			7.7212	155.88	1.83	-
											GLU 114, SER 262,
											TYR 268, TYR 291,
	14	-9.1	5	2.16	2.16	151.84	0.8	11.821	150.85	6.40	GLU 297
	15	-7.0	0	2.16	2.17	151.84	0.8	7.951	156.74	1.5	-
	16	-5.6	0	2.16	2.16	151.84	0.8	7.9606	150.89	4.45	-
	17	-7.1	2	2.16	2.17	151.84	0.8	7.6	155.2	2.6	THR 240, GLY 247
						151.84	0.8				GLU 114, SER 262,
	18	-8.1	3		2.16			10.5309	151.17	5.60	TYR 268, TYR 291
	19	-10.02	3	2.16	2.16	151.84	0.8	12.6803	151.04	6.73	SER 116
2W5Q				2.07		177.84	0.81				
(LtaS)	**13**	-6	1		2.06			7.25	178.03	3.53	ASP 502
	14	-6.2	0	2.07	2.07	177.84	0.81	10.73	177.85	5.36	-
	15	-7.8	1	2.07	2.07	177.84	0.81	7.99	178.05	3.89	ASP 366
	16	-5.7	0	2.07	2.06	177.84	0.81	7.94	176.11	4.83	-
	17	-7.5	1	2.07	2.07	177.84	0.81	7.72	184	0.7	ASP 521
	18	-8.9	2	2.07	2.06	177.84	0.81	10.98	176.25	6.28	GLY 296, GLY 478

	19	-7.5	0	2.07	2.0697	177.84	0.81	9.2	177.15	4.98	-
4WVJ				2.77	2.75	239.62	0.82				
(SpsB)	**13**	-7.3	2					7.26	238.84	4.02	SER 343
	14	-8.3	2	2.77	2.75	239.62	0.82	12.90	237.89	7.31	TYR 182, ALA 330
	15	-9.5	2	2.77	2.76	239.62	0.82	7.76	238.10	4.64	ASP 20
	16	-6.1	0	2.77	2.75	239.62	0.82	8.09	237.67	5.02	-
	17	-7.1	0	2.77	2.76	239.62	0.82	7.70	238.36	4.1	-
	18	-7.5	2	2.77	2.75	239.62	0.82	8.89	238.49	5.01	GLU 51, PRO 340
	19	-8.9	2	2.77	2.74	239.62	0.82	10.14	238.36	5.70	GLU 50, VAL 378
6S7V							0.81				
(LtaA)	**13**	-8.3	1	2.13	2.12	192.79		7.55	190.60	4.87	GLY 259
	14	-8.6	1	2.13	2.12	192.79	0.81	11.06	187.8256	8.01	ILE 256
	15	-10.0	1	2.13	2.12	192.79	0.81	7.91	190.39	5.15	TYR 377
	16	-6.2	0	2.13	2.12	192.79	0.81	7.84	190.33	5.15	-
	17	-8.0	0	2.13	2.12	192.79	0.81	7.8	189.5	3.8	-
	18	-9.7	0	2.13	2.12	192.79	0.81	11.06	189.55	7.15	-
	19	-10.2	2	2.13	2.12	192.79	0.81	9.71	189.48	6.51	ILE 230, TYR 377
6RYP				1.86		108.41	0.82				
(LspA)	**13**	-7.4	1		1.84			7.31	107.33	4.19	GLY 54
	14	-10.0	2	1.86	1.83	108.41	0.82	12.55	105.94	7.51	ASP 136
	15	-10.6	0	1.86	1.84	108.41	0.82	7.91	106.88	4.71	-
	16	-7	0	1.86	1.84	108.41	0.82	7.82	105.99	5.15	-
	17	-8.1	2	1.86	1.85	108.41	0.82	7.5	107.3	4.05	ILE 120, THR 140
	18	-9.2	2	1.86	1.83	108.41	0.82	9.76	106.50	5.83	GLY 54, THR 140
	19	-11.5	1	1.86	1.83	108.41	0.82	10.58	106.47	6.26	THR 140

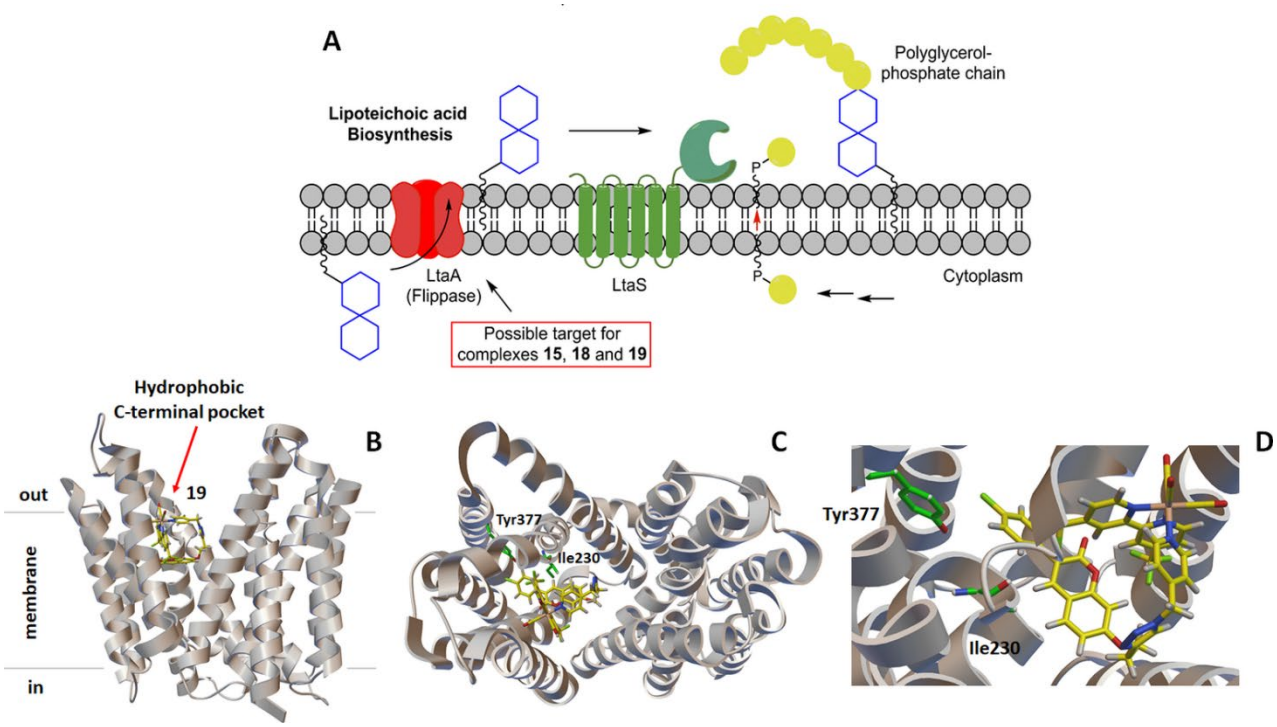

Figure 5. A: schematic diagram of the lipoteichoic acid synthetic machinery in MRSA with possible target of active antimicrobial rhenium complexes. For more details about scheme A, see [81]. Computer-generated lowest energy pose of selected complex **19** in the hydrophobic C-terminal pocket of lipoteichoic acids flippase (LtaA): B: side view; C: top view; D: detail of binding region. In C and D in green are shown the two amino acid residues most likely involved in H-bonding interactions with **19**.

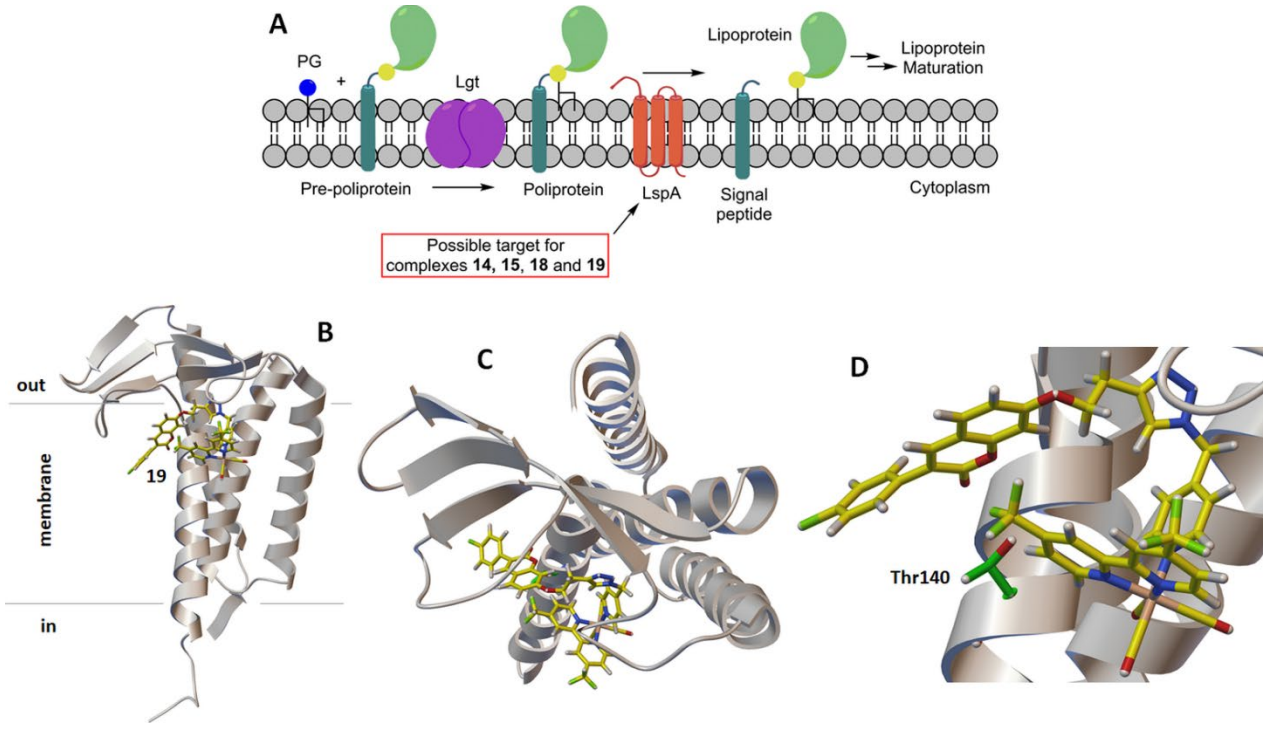

Figure 6. A: schematic diagram of the lipoprotein posttranslational processing pathway with the possible target of active antimicrobial rhenium complexes. For more details about scheme A, see [79]. Computer-generated lowest energy pose of selected complex **19** in in lipoprotein signal peptidase II (LspA): B: side view; C: top view; D: detail of binding region. In C and D in green is shown the amino acid residue most likely involved in H-bonding interactions with **19**.

Finally, in Figures 7 and 8, the hydrophobic gaussian surface was used for the graphical representation of the binding pockets of the ligands. The hydrophobicity scales of Wimley and White was used for defining the hydrophobicity of amino acid residues [97]. This prediction assumes that apolar sites will be disposed preferentially to the molecular interior, forming a hydrophobic core, whereas polar sites will be disposed outside the molecular interior. In Supplementary Materials (Figure S8) the representation for the protein surface of the non-polar polar ratio (NPP) and patch analysis for the electrostatic surface potential are depicted. To analyze the effect on the distortion of the receptor and conformation changes when binding the complex, the results of the Rg for the receptors and the complex are presented in Table 2. As it can be appreciated from the values, the Rgs of the explored systems do not change significantly for any of the shown complexes. The solvent accessible surface area (SASA) was also assessed for all cases. We did not observe intrinsic flexibility changes of receptor SASA and system SASA, which can also be seen from the data in the Table 2. We find, in most cases, that the interfaces gain accessibility in order to promote stable interactions. The localisation of the complexes preserves the SASA which is an indication of the protein stability in the presence and absence of the complexes (i.e. ligands). With this property, we have a clearer picture of the current changes in the protein conformation. The available surface area is kept before and after the docking, and, as intuitively predicted, the rhenium complexes prefer localizing in hydrophobic pockets of the possible target enzymes (Figures 7 and 8).

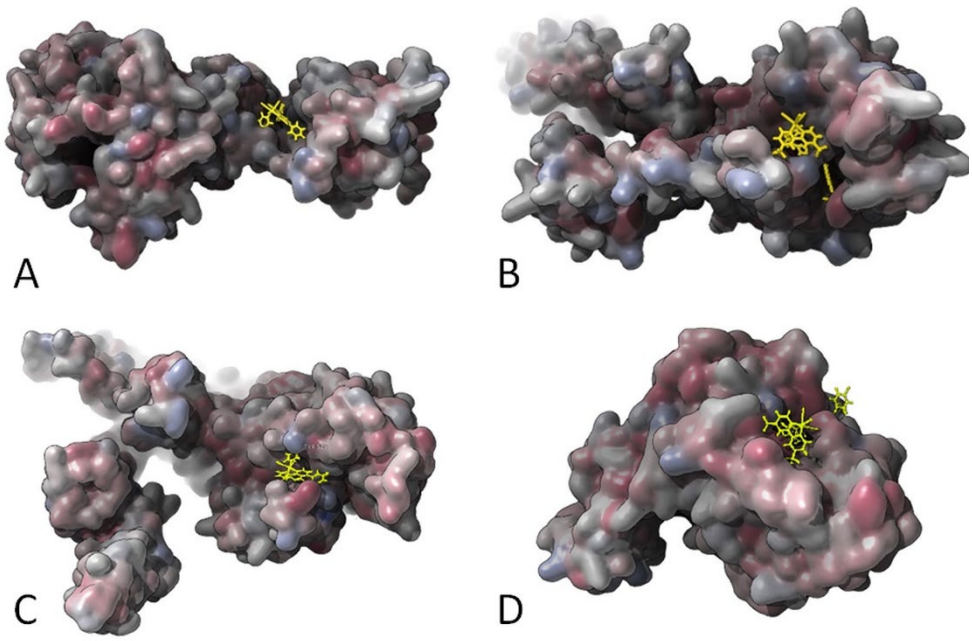

Figure 7. Gaussian surface representation of hydrophobicity of: A. **15** and PBP2 (2OLV); B. **19** and PBP2a (4DKI); C. **15** and PBP3 (3VSL); D. **19** and PBP4 (5TXI). Red-blue color palette changes from hydrophilic blue to hydrophobic red.

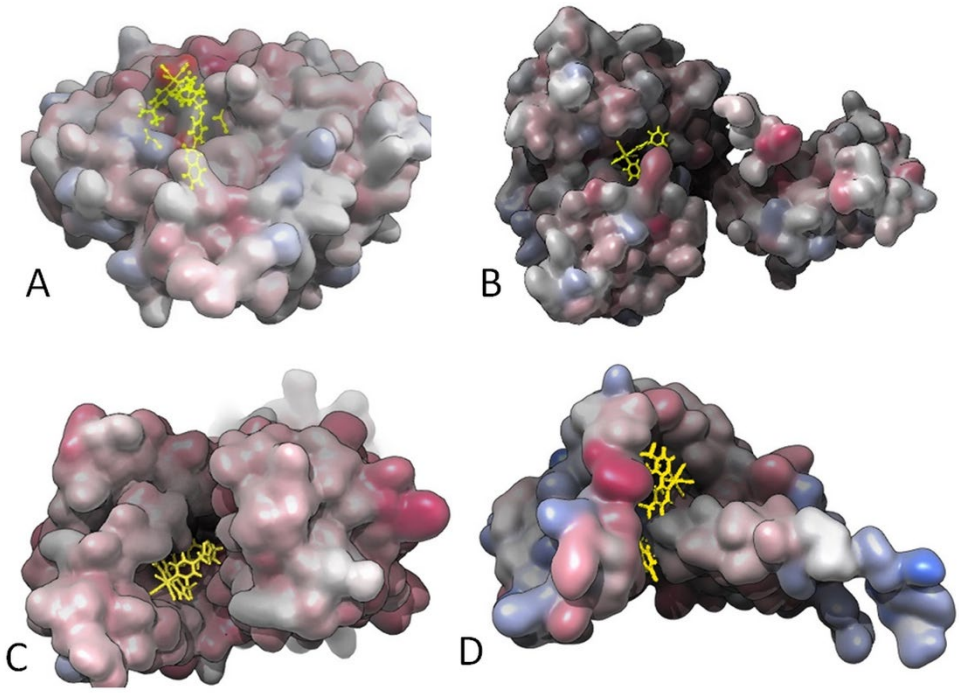

Figure 8. Gaussian surface representation of hydrophobicity of: A. **18** and Lipoteichoic acids synthase (LtaS; 2W5Q); B. **15** and Type-I signal peptidase (SpsB; 4WVJ); C. **19** and Lipoteichoic acids flippase (LtaA) – top view (6S7V); D. **19** and Lipoprotein signal peptidase II (LspA; 6RYP). Red-blue color palette changes from hydrophilic blue to hydrophobic red.

3. Conclusions

In this study, we have reported the synthesis, characterization and antimicrobial effects of a series of rhenium di- and tricarbonyl diimine complexes. Due to the lack of activity of the tested species, and in an effort to identify the possible targets of active complexes (and thus possibly understand the underlying reasons for the observed differences in the antimicrobial efficacy of Re complexes), we computationally evaluated the binding affinity of active and inactive molecules against structurally characterized membrane bound *S. aureus* proteins. Whereas inactive compounds do not show affinity for the enzymes, our docking protocol identified two possible major targets for some molecules of this class of compounds, namely lipoteichoic acids flippase (LtaA) and lipoprotein signal peptidase II (LspA). To our knowledge, our study is the first ever-reported attempt to identify computationally MRSA biological targets for antibiotic metal complexes. Experimental data are needed in the future to confirm the *in silico* results, but out data are in line with the limited mechanistic studies previously published on microbicidal rhenium species. Indeed, if the complexes inhibit the catalytic activity of LtaA and LspA, essential cell wall polymers cannot be assembled leading to microbial death. We emphasize that LtaA and LspA may be targets for a fraction of known active antimicrobial Re complexes (namely **14**, **15**, **18** and **19** in this study). Penicillin-binding protein 2a (PBP2a) might also be targeted by **15** and **19**, while MurG may be inhibited by **17**. We were not able to identify possible targets for compounds **14** and **16**, thus their mechanism of action and targets remain unknown. We also showed that active rhenium complexes tend to localize in hydrophobic pockets of target enzymes. In terms of the key molecular features common to active rhenium carbonyl complexes, our data support the notion that active diimine species are only cationic complexes of the *fac*-$[Re(CO)_3]^+$ core. If a CO ligand is substituted leading to dicarbonyl *cis*-$[Re(CO)_2]^n$, regardless of the overall charge of the compounds, the molecules are devoid of any antimicrobial activity. Arguably, the most significant outcome of our study, i.e. the indication of LtaA and LspA as possible targets for this class of antibiotics, is that of offering the scientific community involved in this research a support for

rational design of rhenium complexes based on the computational protocol for computer-aided drug design.

4. Materials and Methods

4.1. Reagents and chemicals

All reagent and solvents were purchased from standard sources and used without further purification. Compound $[Re(CO)_5Br]$ was purchased from Sigma Aldrich. Complexes $(Et_4N)[Re(CO)_2Br_4]$ [68], **1a-2a** [52], **1b**-**5b** [51], **1c** [98], **9a** [99], **9b** [100], **9c** [101], **10** [49] were synthesized according to published procedures. Unless otherwise noted, solvents used in the preparation of all molecules were dry and O_2-free.

4.2. Instruments and analysis

NMR spectra were measured on a Bruker Advance III 400 MHz. The corresponding ^1H chemical shifts are reported relative to residual solvent protons. Mass analyses were performed using a Bruker FTMS 4.7-T Apex II in positive mode. UV-Vis spectra were measured on a Jasco V730 spectrophotometer. IR spectra were recorded on a Bruker TENSOR II with the following parameters: 16 scans for background, 32 scans for sample with a resolution of 4 cm^{-1} in the 4000-600 cm^{-1} region. Single crystal diffraction data collection was performed on a Stoe IPDS2 diffractometer (CuKα1 (λ = 1.5406 Å)) equipped with a cryostat from Oxford Cryosystems. The structure were solved with the ShelXT structure solution program using Intrinsic Phasing and refined with the ShelXL refinement package using Least Squares minimization [102,103]. All crystal structures are deposited at the Cambridge Crystallographic Data Centre. CCDC numbers 2184717-2184724 contain the supplementary crystallographic data for this paper. These data can be obtained free of charge from the Cambridge Crystallographic Data Centre via www.ccdc.cam.ac.uk/structures.

4.3. Synthetic procedures

$(TDAE)[Re(CO)_2(bpy)Br_2]_2$ (1'). Synthesized according to a published similar procedure [51]. Briefly, $[Re(CO)_2(bpy)Br_2]$ (**1a**, 63.5 mg, 114.0 µmol) was dissolved in dry CH_2Cl_2 (DCM) (20 mL) in a glove box. Tetrakis(dimethylamino)ethylene (TDAE, 13.24 µL, 57.0 µmol, 0.5 eq.) was dissolved in dry DCM (1 mL). The latter solution was added dropwise to the solution of **1a**. The mixture was stirred under inert condition for 15 min. The solvent was removed under reduced pressure giving compound **1'**, as a purple solid. Yield: 71.9 mg, 55.0 µmol, 96%. IR (cm^{-1}), ν_{CO}: 1861, 1775. UV-Vis (DMF), λ_{max} [nm] : 593, 426, 308, 300.

$[Re(CO)_2(bpy)(MeIm)Br]$ (3a). Degassed complex **1'** (35.6 mg, 27.0 µmol) was dissolved in dry toluene (20 mL). Anhydrous *N*-methyl imidazole (MeIm, 4.32 µL, 54 µmol, 2 eq.) was added and the mixture was stirred at 100 °C for 48 h. The mixture was cooled down to room temperature and the brown precipitate was isolated by centrifugation giving compound **3a**. Yield: 15.8 mg, 28.1 µmol, 52%. Single crystals suitable for X-ray diffraction were grown by layering pentane on a CH_2Cl_2 solution of the compound giving dark brown crystals. IR (cm^{-1}), ν_{CO}: 1877, 1779. ESI-MS (MeOH) : *m*/*z*, 582.9 $[M + Na]^+$.

$[Re(CO)_2(bpy)(py)_2]PF_6$ (4a). Synthesized according to a published similar procedure [51]. Briefly, complex **2a** (54 mg, 97 µmol) and pyridine (py, 1 mL, ca. 100 eq.) were dissolved in MeOH (20 mL) and the mixture was stirred at 70 °C overnight. The solvent was removed under reduced pressure. The residue was dissolved in water (75 mL) and a solution of KPF_6 (36 mg, 194 µmol, 2 eq.) in water (5 mL) was added dropwise to the rhenium. The precipitate was isolated by centrifugation giving compound **4a** as a brown-orange solid. Yield: 45 mg, 64.1 µmol, 66%. Single crystals suitable for X-ray diffraction were grown by a diffusion of pentane into an acetone solution of the compound giving dark orange crystals. IR (cm^{-1}), ν_{CO}: 1901, 1823. UV-Vis (DMF), λ_{max} [nm] : 481, 357, 302. ^1H NMR (400 MHz, CD_2Cl_2, ppm) δ : 9.32 (ddd, J = 0.73, 1.56, 5.41 Hz, 2H), 8.36 - 8.40 (m, 4H), 8.34 (d, J = 8.19 Hz, 2H), 8.18 (dt, J = 1.59, 7.95 Hz, 2H), 7.74 (ddd, J = 1.28, 5.47, 7.67 Hz, 2H), 7.59 - 7.65 (m, 2H), 7.05 - 7.11 (m, 4H). ^{13}C NMR (101 MHz, CD_2Cl_2, ppm) δ : 205.9

(2C), 156.6 (2C), 155.3 (4C), 152.5 (2C), 141.1 (2C), 137.6 (2C), 129.3 (2C), 126.5 (4C), 125.1 (2C). ESI-MS (MeOH) : *m*/*z*, 556.7 $[M]^+$.

$[Re(CO)_2(bpy)(MeIm)_2]PF_6$ (5a). Compound **1'** (132 mg, 100 μmol) was dissolved in anhydrous MeIm (8 mL) and the mixture was stirred at 110 °C for 60 min. The solvent was removed under reduced pressure and the residue was purified by flash column chromatography (eluent: EtOAc 100%, then DCM/MeOH 100:0, increased to 98:2). The first fraction, compound **3a**, was collected with the first gradient (100% EtOAc) as a brown solid (amount: traces). The second fraction was collected with the last gradient as mobile phase. Once dried, the counterion was exchanged with KPF_6 (17.2 mg, 93.4 μmol) in H_2O (15 mL). Complex **5a** was isolated by centrifugation as a violet solid. Yield: 24 mg, 33.9 μmol, 17%. IR (cm^{-1}), ν_{CO}: 1885, 1802. UV-Vis (DMF), λ_{max} [nm] : 500, 363, 307, 300. ^1H NMR (400 MHz, CD_2Cl_2, ppm) δ : 9.21 - 9.26 (m, 2H), 8.32 (dd, J = 0.86, 8.19 Hz, 2H), 8.12 (dt, J = 1.59, 7.95 Hz, 2H), 7.62 (ddd, J = 1.22, 5.44, 7.64 Hz, 2H), 7.29 (s, 2H), 6.63 - 6.67 (t, 2H), 6.44 - 6.51 (t, 2H), 3.53 (s, 6H). ^{13}C NMR (101 MHz, CD_2Cl_2, ppm) δ : 207.6 (2C), 156.7 (2C), 152.5 (2C), 141.2 (2C), 140.4 (2C), 132.0 (2C), 128.6 (2C), 124.5 (2C), 122.3 (2C), 34.7 (2C). ESI-MS (MeOH) : *m*/*z*, 562.7 $[M]^+$.

$(TDAE)[Re(CO)_2(phen)Br_2]_2$ (1''). Synthesized according to a published similar procedure [51]. Briefly, cis-$[Re(CO)_2(phen)Br_2]$ (62.8 mg, 107.9 μmol) was dissolved in dry DCM (17 mL) in a glove box. TDAE (12.56 μL, 53.9 μmol, 0.5 eq.) was dissolved in dry DCM (1.5 mL). The latter solution was added dropwise to the rhenium in the glove box and the mixture was stirred for 15 min at room temperature. The solvent was removed under reduced pressure giving **1''** as a brown-purple solid. Yield: 67.7 mg, 49.6 μmol, 92%. IR (cm^{-1}), ν_{CO}: 1856, 1771.

$[Re(CO)_2(phen)(py)Br]$ (2c). Degassed complex **1''** (20 mg, 14.7 μmol) was dissolved in degassed pyridine (2 mL) and the mixture was stirred at 100 °C for 20 min. The reaction mixture was cooled down to room temperature and extracted in DCM (50 mL) with HCL 0.1 M (3 x 50 mL). The organic phase was dried over sodium sulfate and the solvent was removed under reduced pressure. The crude was purified by flash column chromatography (stationary phase: Aluminum oxide, mobile phase: Pentane / EtOAc / MeOH 1:2:0, increased to 0:1:0 and finally 0:99:1) giving compound **2c** as a brown solid. Yield: 0.9 mg, 1.6 μmol, 5%. IR (cm^{-1}), ν_{CO}: 1864, 1778.

$[Re(CO)_2(phen)(MeIm)Br]$ (3c). Degassed complex **1''** (17 mg, 12.5 μmol) was dissolved in anhydrous MeIm (2 mL) and the mixture was stirred at 110 °C for 20 min. The reaction mixture was cooled down to room temperature and extracted in DCM (50 mL) with HCl 0.1 M (3 x 50 mL). The organic phase was dried over sodium sulfate and the solvent was removed under reduced pressure. The crude was purified by flash column chromatography (stationary phase: Aluminum oxide, mobile phase: Pentane / EtOAc 1:1, increased to 0:1) giving compound **3c** as a violet solid. Yield: 1.8 mg, 3.1 μmol, 12%. IR (cm^{-1}), ν_{CO}: 1876, 1773.

The following general procedure was applied for the synthesis of complexes **6-8** [50]. To a solution of $[Re(CO)_5Br]$ (1.0 equiv.) in hot toluene, the appropriate bipyridine (bpy) ligand (1.0 equiv.) was added, and the mixture refluxed for 7–9h. After the solution had cooled to the room temperature, the reaction mixture was filtered and washed with cold toluene (2×), yielding *fac*-$[Re(CO)_3(bpy)Br]$ as a bright fluorescent yellow powder. The solid was then dried in vacuo for 24h. Complexes were found to be pure (≥ 96%) by NMR and HPLC.

***fac*-$[Re(CO)_3(^tBu\text{-}bpy)Br]$ (6)**. Where ^{t}Bu-bpy is 4,4'-di-tert-butyl-2,2'-bipyridine. Pale yellow solid, yield 92%. IR (solid, cm^{-1}); νCO: 2016, 1912, 1889, 1869. UV-Vis (DMF), λ_{max} [nm] : 368, 292. ^1H-NMR (400 MHz, CD_3CN, ppm): 8.96 (d, J=5.99 Hz, 2H) 8.10 (d, J=1.71 Hz, 2H) 7.51 (dd, J=5.87, 1.96 Hz, 2H) 1.45 (s, 18H). ESI^+-MS (MeOH): m/z, 576.9 $[Re(CO)_3(C_{18}H_{24}N_2)(H_2O)]^+$, $[M\text{-}Br+H_2O]^+$. Single crystals suitable for X-ray diffraction were grown by diffusion of pentane into a DCM solution of the compound giving yellow needles.

***fac*-[Re(CO)$_3$(CF$_3$-bpy)Br] (7)**. Where CF$_3$-bpy is 4,4'-bis(trifluoromethyl)-2,2'-bipyridine. Orange solid, yield 87%. IR (solid, cm^{-1}); νCO: 2015, 1932, 1897. UV-Vis (DMF), λ_{max} [nm] : 417, 304. ^{1}H-NMR (400 MHz, CD$_3$CN, ppm): 9.33 (d, J=5.75 Hz, 2H) 8.46 (s, 2H) 7.84 (dd, J=5.75, 1.22 Hz, 2H). ESI$^+$-MS (MeOH): m/z, 580.7 [Re(CO)$_3$(C$_{12}$H$_6$F$_6$N$_2$)(H$_2$O)]$^+$, [M-Br+H$_2$O]$^+$. Single crystals suitable for X-ray diffraction were grown by diffusion of hexane into a DCM solution of the compound giving orange needles.

***fac*-[Re(CO)$_3$((Et)$_2$N-bpy)Br] (8)**. Where (Et)$_2$N-bpy is N4,N4,N4',N4'-tetraethyl-[2,2'-bipyridine]-4,4'-diimine. Pale yellow solid, yield 92%. IR (solid, cm^{-1}); νCO: 2008, 1886, 1866. UV-Vis (DMF), λ_{max} [nm] : 367, 373. ^{1}H-NMR (400 MHz, CD$_3$CN, ppm): 8.49 (d, J=6.60 Hz, 2H) 7.04 (d, J=2.81 Hz, 2H) 6.54 (dd, J=6.72, 2.69 Hz,2H) 3.49 (q, J=7.21 Hz, 8H) 1.28 (t, J=7.21 Hz, 12 H). ESI$^+$-MS (MeOH): m/z, 568.9 [Re(CO)$_3$(C$_{18}$H$_{26}$N$_4$)]$^+$, [M-Br]$^+$. Single crystals suitable for X-ray diffraction were grown by diffusion of pentane into a DCM solution of the compound giving yellow needles.

***cis*-[Re(CO)$_2$(batho-phen)Br$_2$] (11).** Degassed (Et$_4$N)[Re(CO)$_2$Br$_4$] (500 mg, 722 μmol) and batho-phen (240 mg, 722 μmol) were dissolved in dry DCM (80 mL). The mixture was stirred under inert conditions at room temperature for 72 h. The solvent was removed under reduced pressure and the crude was purified by flash column chromatography on silica (Eluent: DCM / Pentane 1:9), giving complex **11** as an orange-red solid. Yield: 82 mg, 112 μmol, 15%. Single crystals suitable for X-ray diffraction were grown by slow evaporation of DCM solution of the compound giving dark brown needles. IR (cm^{-1}), νCO: 1999, 1849. UV-Vis (DMF), λ_{max} [nm]: 429, 288.

4.4. Biological Tests

4.4.1 Strains and culture conditions.

Antimicrobial activity was evaluated against 8 different microorganisms including four Gram-negative bacteria (*Enterobacter cloaceae* ATCC 3047, *Klebsiella pneumoniae* ATCC 13803, *Acinetobacter baumanii* ATCC 19606, *Pseudomonas aeruginosa* PAO1 NCTC10332), two Gram-positive bacteria (*Staphylococcus aureus* MRSA43300 (methicillin-resistant) and *S. aureus* ATCC25923 (methicillin-sensitive)) and two fungi (*Candida albicans* SC5314) and *C. auris* (a clinical strain). All reference strains were obtained from the American Type Culture Collection (ATCC) and the National Collection of Type Cultures (NCTC), while a clinical *C. auris* strain 7 was kindly provided by Dr Aleksandra Barac (University Clinical Center of Serbia) and prof. Cornelia Lass-Floerl (University of Innsbruck). Prior to each experiment, frozen stocks in 20% glycerol at -80 °C were thawed and inoculated onto solid Yeast-Potato Dextose (YPD) plates (fungi) or Lauria (LA) agar plates (bacteria), and cultured at 37 °C for 24-48 h.

4.4.2 In vitro antimicrobial activity determination.

Antimicrobial activity was addressed by determining the minimum inhibitory concentration (MIC) of the tested complexes according to the standard broth microdilution assays, recommended by CLSI (the Clinical and Laboratory Standards Institute; M07-A10. CLSI) and EUCAST (European Committee on Antimicrobial Susceptibility Testing; EUCAST antifungal MIC method for yeasts, v 7.3.1). The test strains grown in YPD (fungi) and LA (bacteria) were diluted in RPMI 1640 medium with 2% glucose (Gibco) and Luria-Bertani broth (Biolife Italiana S.r.l., Milano, Italy) to give the concentration of 1x105 CFU/mL cells (for fungi) and 5x105 CFU/mL (for bacteria), respectively. The MIC assay was performed in 96-well microtiter plates (Sarstedt, Germany) by making serial twofold dilutions of the tested substances in appropriate liquid media to give the volume of 100 μL. The media solution with microorganisms was dispensed to each well to make the final volume of 200 μL. All complexes were tested in the concentrations range from 100 to 3.13 μM. After incubation at 37 °C for 18-24 h without shaking, the growth of tested microorganisms was determined measuring absorbance at 530 nm (fungi) and 600 nm (bacteria) using a Tecan Infinite 200 Pro multiplate reader (Tecan Group Ltd., Männedorf, Switzerland). The negative control (media only) and positive control (only microorganisms) on the same plate

were used as references to determine the growth inhibition. Samples with inhibition values above 90% were classified as active agents.

4.5. In silico calculations

4.5.1 Preparation of the ligand database and ligands – receptors complexes.

Docking calculations were performed with AutoDock Vina version 1.2.0 (The Scripps Research Institute, La Jolla, San Diego, USA) [14] and AutoDock4 version 4.2.6 (AD4, The Scripps Research Institute, La Jolla, San Diego, USA) [104]. The receptor/protein.PDBQT files were prepared, and the grid box size was determined using the AutoDock Tools version 1.5.7 (ADT; Scripps Research Institute, La Jolla, San Diego, USA) [104]. Biovia Discovery Studio Visualizer 2021, version 21.1.0.20298 (Dassault Systèmes, San Diego, California, USA) was used to visualize receptor and ligand interactions. Figures were prepared with the ADT software. Structures of complexes **5**-**11** and **15**, were obtained by the determined x-ray structures. Chemical structures as .CIF files were converted to .MOL2 files using the Mercury (Build RC1) version 3.7 (CCDC 2001-2015) software. All complexes (ligands) were optimized with the The hybrid meta-GGA functional wB97XD [105-109] designed to account for dispersion, was used in combination with the standard SDD basis sets [110]. The optimized structures were subject to frequency analysis to verify that they represent minima on the potential energy surface. All calculations were performed with Gaussian 09 software (version 5.0.9, Carnegie Mellon University, Gaussian, Inc.).

The ADT software was then used to investigate the complexes' structures in terms of combinations with nonpolar hydrogens, additions of Gasteiger changes, and rotatable bonds. The rhenium atom is not parametrized in AD4 and AutoDock Vina, thus AutoDock Vina calculations were performed using Mn instead of Re. The resulting binding poses of the Mn complexes were then cross-checked with corresponding Re complexes using AD4 where the following line was added to the AD4 atom parameters file: "atom_par Re 2.95 0.066 12.000 -0.00110 0.0 0.0 0 -1 -1 1 # Non H-bonding". The binding poses of the Mn and Re complexes were found to be the same. Also, due to the fact that ADT failed to assigned a Gasteiger change to the metal ion, a charge of 0.320 (to either Mn or Re) was assigned to the atom by editing the corresponding .PDBQT file [111].

The crystal structure of S. aureus proteins were obtained from the RCSB protein data bank (http://www.rcsb.org). Only structures of membrane protein annotation (PDBTM, MemProtMD, OPM or mpstruc) were considered and selected. All water molecules were removed, and the required files for AutoDock Vina and AD4 were prepared by assigning hydrogens and Kollman charges to protein structures, and finally converting them from the .PDB file format to .PDBQT file format.

4.5.2. Molecular docking.

The docking calculations were conducted using the AutoDock Vina software (https://vina.scripps.edu/) with adapted parameters for the rhenium complexes. The extended version of the Vina code was used via the integrated platform SAMSON [https://www.samson-connect.net] as a SAMSON extension [112]. It provides additional functionality for preparing receptors and ligands, docking libraries, analyzing docking results, and exporting them. Both the number of flexible side chains and the size of the search domain were different for all the cases because of the receptor's conformation (i.e. chain orientation, position of residues). On average, there were about 30 flexible side chains with unlocked rotatable bonds. The search space was defined by a docking box wrapper the space around the receptors. The scaling of the box depending of the defines pocket score. The number of modes were set to 200 with energy range = 3 kcal/mol (default value) The energy range is a maximum energy difference between the best binding mode and the unfavourable one displayed (kcal/mol). The energy (affinity) that differs more than 3 kcal/mol from the best mode are not saved among results. In the configuration file the parameter called "exhaustiveness" was set to 40. This parameters controls how comprehensive will be the search space. In AutoDock Vina the electrostatic interactions were

handled with the hydrophobic and the hydrogen bonding terms. interactions were handled with the hydrophobic and the hydrogen bonding terms. Post-docking analysis approach for the favorable ligands-receptors complex was performed via the Protein-Ligand Interaction Analyzer Extension in SAMSON [112]. With the help of Protein-Ligand Interaction Analyzer, it was possible to calculate the radius of gyration, hydrogen bonds, residues surrounding the ligand, and solvent-accessible surface area (SASA) from the receptor and the ligand, and for the form complexes. The multistep validation protocol were considered in this study, and the ability of combined methodology was examined independently with initial screening and the extensive semi-flexible docking.

Supplementary Materials: Figures S1-S5: ^{1}H-NMR spectra of compounds; Figures S6: IR spectra (solid state) of compounds; Figures S7: UV-Vis spectra (in DMF) of compounds; Figures S8: Visualisation of surface protein surface polarity (A) non-polar to polar SASA colour-coded from low NPP ratio (purple) to high NPP ratio (green), and in (B) colour-coded from negative charge (red) to positive charge (blue). Regions of high hydrophobicity are coloured green, low hydrophobicity coloured purple; Figures S9a: Binding orientation of the compounds with hydrogen-acceptor and hydrogen-donor distances: A. 15 and PBP2 : 2OLV ; B. 19 and PBP2a : 4DKI ; C. 15 and PBP3: 3VSL; D. 19 and PBP4: 5TXI; Figures S9b: Binding orientation of the compounds with hydrogen-acceptor and hydrogen-donor distances: A. 18 and Lipoteichoic acids synthase (LtaS): 2W5Q; B. 15 and Type-I signal peptidase (SpsB): 4WVJ; C. 19 and Lipoteichoic acids flippase (LtaA): 6S7V; D. 19 and Lipoprotein signal peptidase II (LspA): 6RYP; Table S1a: *In silico* pre-screening of binding affinities (*b.a.*; docking scores. kcal/mol) of rhenium complexes against structurally characterized membrane bound *S. aureus* proteins: Penicillin Binding Proteins (PBPs); Table S1b: *In silico* pre-screening of binding affinities (b.a.; docking scores. kcal/mol) of non-toxic complexes against other structurally characterized membrane bound *S. aureus* proteins; Table S2: Pockets prediction – mapping the ranking with residues environment distribution; Table S3: Histogram of percentage distribution of the surrounding residue types for the two groups of protein.

Author Contributions: Conceptualization, F.Z. and M.N.; methodology, M.N. and F.Z..; software, N.M., A.C., M.L. and F.Z.; validation, N.M., A.C., A.P., and F.Z.; formal analysis, K.S, Y.C., N.M., A.C., A.P. and F.Z..; investigation, K.S, Y.C., N.M., A.C., A.P. and F.Z.; resources, M.L., A.P. and F.Z.; data curation, K.S, Y.C., N.M., A.C., A.P. and F.Z.; writing—original draft preparation, K.S, Y.C., N.M., A.P. and F.Z.; writing—review and editing, all authors; visualization, N.M., A.C., A.P. and F.Z.; supervision, M.L., A.P. and F.Z..; project administration, A.P. and F.Z.; funding acquisition, F.Z. All authors have read and agreed to the published version of the manuscript.

Funding: This research was funded by Swiss National Science Foundation (Project# 200021_196967), and Ministry of Education, Science and Technological Development of the Republic of Serbia (Project No. 451-03-9/2021-14/200042, 2021).

Data Availability Statement: In this section, please provide details regarding where data supporting reported results can be found, including links to publicly archived datasets analyzed or generated during the study. Please refer to suggested Data Availability Statements in section "MDPI Research Data Policies" at https://www.mdpi.com/ethics. If the study did not report any data, you might add "Not applicable" here.

Acknowledgments: Financial support from the Fonds de recherche du Centenaire de l'Université de Fribourg (Project No. 818), and National Competence Centre for Research (NCCR), "Bioinspired Materials" is gratefully acknowledged.

Conflicts of Interest: The authors declare no conflict of interest.

References

1. WHO. *Global shortage of innovative antibiotics fuels emergence and spread of drug-resistance*; 2021; p 1.
2. Hu, Q.; Cheng, H.; Yuan, W.; Zeng, F.; Shang, W.; Tang, D.; Xue, W.; Fu, J.; Zhou, R.; Zhu, J., et al. Panton-Valentine leukocidin (PVL)-positive health care-associated methicillin-resistant Staphylococcus aureus isolates are associated with skin and soft tissue infections and colonized mainly by infective PVL-encoding bacteriophages. *J. Clin. Microbiol.* **2015**, *53*, 67-72, doi:10.1128/JCM.01722-14.

3. Tong, S.Y.C.; Davis, J.S.; Eichenberger, E.; Holland, T.L.; Fowler, V.G. Staphylococcus aureus Infections: Epidemiology, Pathophysiology, Clinical Manifestations, and Management. *Clin. Microbiol. Rev.* **2015**, *28*, 603-661, doi:doi:10.1128/CMR.00134-14.
4. Laupland, K.B.; Lyytikäinen, O.; Sgaard, M.; Kennedy, K.J.; Knudsen, J.D.; Ostergaard, C.; Galbraith, J.C.; Valiquette, L.; Jacobsson, G.; Collignon, P., et al. The changing epidemiology of Staphylococcus aureus bloodstream infection: a multinational population-based surveillance study. *Clin. Microbiol. Infect.* **2013**, *19*, 465-471, doi:https://doi.org/10.1111/j.1469-0691.2012.03903.x.
5. Plackett, B. Why big pharma has abandoned antibiotics. *Nature* **2020**, *586*, S50-S52, doi:https://doi.org/10.1038/d41586-020-02884-3.
6. Yu, W.; MacKerell, A.D., Jr. Computer-Aided Drug Design Methods. *Methods Mol. Biol.* **2017**, *1520*, 85-106, doi:10.1007/978-1-4939-6634-9_5.
7. Rao, Q.; Shang, W.; Hu, X.; Rao, X. Staphylococcus aureus ST121: a globally disseminated hypervirulent clone. *J. Med. Microbiol.* **2015**, *64*, 1462-1473, doi:https://doi.org/10.1099/jmm.0.000185.
8. Yu, W.; Lakkaraju, S.K.; Raman, E.P.; Fang, L.; MacKerell, A.D. Pharmacophore Modeling Using Site-Identification by Ligand Competitive Saturation (SILCS) with Multiple Probe Molecules. *J. Chem. Inf. Model.* **2015**, *55*, 407-420, doi:10.1021/ci500691p.
9. Nedyalkova, M.; Simeonov, V. Partitioning Pattern of Natural Products Based on Molecular Properties Descriptors Representing Drug-Likeness. *Symmetry* **2021**, *13*, 546, doi:10.3390/sym13040546.
10. Barazorda-Ccahuana, H.L.; Nedyalkova, M.; Mas, F.; Madurga, S. Unveiling the Effect of Low pH on the SARS-CoV-2 Main Protease by Molecular Dynamics Simulations. *Polymers* **2021**, *13*, 3823, doi:10.3390/polym13213823.
11. Ustach, V.D.; Lakkaraju, S.K.; Jo, S.; Yu, W.; Jiang, W.; MacKerell, A.D. Optimization and Evaluation of Site-Identification by Ligand Competitive Saturation (SILCS) as a Tool for Target-Based Ligand Optimization. *J. Chem. Inf. Model.* **2019**, *59*, 3018-3035, doi:10.1021/acs.jcim.9b00210.
12. Gaieb, Z.; Parks, C.D.; Chiu, M.; Yang, H.; Shao, C.; Walters, W.P.; Lambert, M.H.; Nevins, N.; Bembenek, S.D.; Ameriks, M.K., et al. D3R Grand Challenge 3: blind prediction of protein–ligand poses and affinity rankings. *J. Comput. Aided Mol. Des.* **2019**, *33*, 1-18, doi:10.1007/s10822-018-0180-4.
13. Forli, S.; Huey, R.; Pique, M.E.; Sanner, M.F.; Goodsell, D.S.; Olson, A.J. Computational protein–ligand docking and virtual drug screening with the AutoDock suite. *Nat. Protoc.* **2016**, *11*, 905-919, doi:10.1038/nprot.2016.051.
14. Trott, O.; Olson, A.J. AutoDock Vina: improving the speed and accuracy of docking with a new scoring function, efficient optimization, and multithreading. *J. Comput. Chem.* **2010**, *31*, 455-461, doi:10.1002/jcc.21334.
15. Śledź, P.; Caflisch, A. Protein structure-based drug design: from docking to molecular dynamics. *Curr. Opin. Struct. Biol.* **2018**, *48*, 93-102, doi:https://doi.org/10.1016/j.sbi.2017.10.010.
16. Cournia, Z.; Allen, B.; Sherman, W. Relative Binding Free Energy Calculations in Drug Discovery: Recent Advances and Practical Considerations. *J. Chem. Inf. Model.* **2017**, *57*, 2911-2937, doi:10.1021/acs.jcim.7b00564.
17. Verma, A.K.; Ahmed, S.F.; Hossain, M.S.; Bhojiya, A.A.; Mathur, A.; Upadhyay, S.K.; Srivastava, A.K.; Vishvakarma, N.K.; Barik, M.; Rahaman, M.M., et al. Molecular docking and simulation studies of flavonoid compounds against PBP-2a of methicillin-resistant Staphylococcus aureus. *J. Biomol. Struct. Dyn.* **2021**, 10.1080/07391102.2021.1944911, 1-17, doi:10.1080/07391102.2021.1944911.
18. Kulanthaivel, L.; Jeyaraman, J.; Biswas, A.; Subbaraj, G.K.; Santhoshkumar, S. Identification of potential inhibitors for Penicillinbinding protein (PBP) from Staphylococcus aureus. *Bioinformation* **2018**, *14*, 471-476, doi:10.6026/97320630014471.

19. Chomnawang, M.T.; Surassmo, S.; Wongsariya, K.; Bunyapraphatsara, N. Antibacterial Activity of Thai Medicinal Plants against Methicillin-resistant Staphylococcus aureus. *Fitoterapia* **2009**, *80*, 102-104, doi:https://doi.org/10.1016/j.fitote.2008.10.007.
20. Alhadrami, H.A.; Hamed, A.A.; Hassan, H.M.; Belbahri, L.; Rateb, M.E.; Sayed, A.M. Flavonoids as Potential anti-MRSA Agents through Modulation of PBP2a: A Computational and Experimental Study. *Antibiotics* **2020**, *9*, 562, doi:10.3390/antibiotics9090562.
21. Aisha, A.; Zahra, S.; Tahir, I.M.; Hussain, A.; Bano, N.; Roobi, A.; Afsheen, N.; Saleem, Y. Anticancer L-Asparaginase and Phytoactive Compounds From Plant Solanum nigrum Against MDR (Methicillindrug resistant) Staphylococcus aureus and Fungal Isolates. *Dose Response* **2022**, *20*, 15593258221092379, doi:10.1177/15593258221092379.
22. Liang, M.; Ge, X.; Xua, H.; Ma, K.; Zhang, W.; Zan, Y.; Efferth, T.; Xue, Z.; Hua, X. Phytochemicals with activity against methicillin-resistant Staphylococcus aureus. *Phytomedicine : international journal of phytotherapy and phytopharmacology* **2022**, *100*, 154073, doi:10.1016/j.phymed.2022.154073.
23. de Oliveira, D.M.; de Oliveira, D.B.C.; Nunes, Y.R.F.; de Almeida Alves, T.M.; Kohlhoff, M.; Andrade, A.A.; Cota, B.B. Natural Occurring Phenolic Derivatives from Mauritia flexuosa (Buriti) Stems and Their Potential Antibacterial Activity against Methicillin-Resistant Staphylococcus aureus (MRSA). *Chem. Biodiversity* **2022**, *19*, e202100788, doi:https://doi.org/10.1002/cbdv.202100788.
24. WHO. *2020 antibacterial agents in clinical and preclinical development: an overview and analysis*; 2021; pp 1-76.
25. Nasiri Sovari, S.; Zobi, F. Recent Studies on the Antimicrobial Activity of Transition Metal Complexes of Groups 6–12. *Chemistry* **2020**, *2*, 418-452, doi:10.3390/chemistry2020026.
26. Frei, A. Metal Complexes, an Untapped Source of Antibiotic Potential? *Antibiotics* **2020**, *9*, 90, doi:10.3390/antibiotics9020090.
27. Patra, M.; Gasser, G.; Metzler-Nolte, N. Small organometallic compounds as antibacterial agents. *Dalton Trans.* **2012**, *41*, 6350-6358, doi:10.1039/c2dt12460b.
28. Sierra, M.A.; Casarrubios, L.; de la Torre, M. Bio-Organometallic Derivatives of Antibacterial Drugs. *Chem. Eur. J.* **2019**, *25*, 7232-7242.
29. Frei, A.; Zuegg, J.; Elliott, A.G.; Baker, M.; Braese, S.; Brown, C.; Chen, F.; C, G.D.; Dujardin, G.; Jung, N., et al. Metal complexes as a promising source for new antibiotics. *Chem. Sci.* **2020**, *11*, 2627-2639, doi:10.1039/c9sc06460e.
30. Li, F.; Collins, J.G.; Keene, F.R. Ruthenium complexes as antimicrobial agents. *Chem. Soc. Rev.* **2015**, *44*, 2529-2542, doi:10.1039/C4CS00343H.
31. Wenzel, M.; Patra, M.; Senges, C.H.; Ott, I.; Stepanek, J.J.; Pinto, A.; Prochnow, P.; Vuong, C.; Langklotz, S.; Metzler-Nolte, N., et al. Analysis of the mechanism of action of potent antibacterial hetero-tri-organometallic compounds: a structurally new class of antibiotics. *ACS Chem. Biol.* **2013**, *8*, 1442-1450, doi:10.1021/cb4000844.
32. Patra, M.; Wenzel, M.; Prochnow, P.; Pierroz, V.; Gasser, G.; Bandow, J.E.; Metzler-Nolte, N. An organometallic structure-activity relationship study reveals the essential role of a Re(CO)3 moiety in the activity against gram-positive pathogens including MRSA. *Chem. Sci.* **2015**, *6*, 214-224, doi:10.1039/c4sc02709d.
33. Siegmund, D.; Lorenz, N.; Gothe, Y.; Spies, C.; Geissler, B.; Prochnow, P.; Nuernberger, P.; Bandow, J.E.; Metzler-Nolte, N. Benzannulated Re(I)-NHC complexes: synthesis, photophysical properties and antimicrobial activity. *Dalton Trans.* **2017**, *46*, 15269-15279, doi:10.1039/c7dt02874a.
34. Frei, A.; Amado, M.; Cooper, M.A.; Blaskovich, M.A.T. Light-activated Rhenium Complexes with Dual Mode of Action against Bacteria. *Chem. Eur. J.* **2019**, *26*, 2852-2858, doi:10.1002/chem.201904689.
35. Zampakou, M.; Akrivou, M.; Andreadou, E.G.; Raptopoulou, C.P.; Psycharis, V.; Pantazaki, A.A.; Psomas, G.J.J.o.i.b. Structure, antimicrobial activity, DNA-and albumin-binding of manganese (II) complexes with the quinolone antimicrobial agents oxolinic acid and enrofloxacin. *J. Inorg. Biochem.* **2013**, *121*, 88-99.

36. Arthi, P.; Shobana, S.; Srinivasan, P.; Prabhu, D.; Arulvasu, C.; Rahiman, A.K.J.J.o.P.; Biology, P.B. Dinuclear manganese (II) complexes of hexaazamacrocycles bearing N-benzoylated pendant separated by aromatic spacers: Antibacterial, DNA interaction, cytotoxic and molecular docking studies. *J. Photoch. Photobio. B* **2015**, *153*, 247-260.
37. Simpson, P.V.; Nagel, C.; Bruhn, H.; Schatzschneider, U. Antibacterial and Antiparasitic Activity of Manganese(I) Tricarbonyl Complexes with Ketoconazole, Miconazole, and Clotrimazole Ligands. *Organometallics* **2015**, *34*, 3809-3815.
38. Boubakri, L.; Mansour, L.; Harrath, A.; Özdemir, I.; Yaşar, S.; Hamdi, N.J.J.o.C.C. N-Heterocyclic carbene-Pd (II)-PPh3 complexes as a new highly efficient catalyst system for the Sonogashira cross-coupling reaction: Synthesis, characterization and biological activities. *J. Coord. Chem.* **2018**, *71*, 183-199.
39. Kaushal, M.; Lobana, T.S.; Nim, L.; Bala, R.; Arora, D.S.; Garcia-Santos, I.; Duff, C.E.; Jasinski, J.P.J.N.J.o.C. Synthesis of 2-acetylpyridine-N-substituted thiosemicarbazonates of copper (II) with high antimicrobial activity against methicillin resistant S. aureus, K. pneumoniae 1 and C. albicans. *New J. Chem.* **2019**, *43*, 11727-11742.
40. Abu Ali, H.; Omar, S.N.; Darawsheh, M.D.; Fares, H.J.J.o.C.C. Synthesis, characterization and antimicrobial activity of zinc (II) ibuprofen complexes with nitrogen-based ligands. *J. Coord. Chem.* **2016**, *69*, 1110-1122.
41. Kumar, S.V.; Scottwell, S.Ø.; Waugh, E.; McAdam, C.J.; Hanton, L.R.; Brooks, H.J.; Crowley, J.D.J.I.C. Antimicrobial properties of tris (homoleptic) ruthenium (II) 2-Pyridyl-1, 2, 3-triazole "click" complexes against pathogenic bacteria, including methicillin-resistant staphylococcus aureus (MRSA). *Inorg. Chem.* **2016**, *55*, 9767-9777.
42. van Hilst, Q.V.C.; Vasdev, R.A.S.; Preston, D.; Findlay, J.A.; Scottwell, S.Ø.; Giles, G.I.; Brooks, H.J.L.; Crowley, J.D. Synthesis, Characterisation and Antimicrobial Studies of some 2,6-bis(1,2,3-Triazol-4-yl)Pyridine Ruthenium(II) "Click" Complexes. *Asian J. Org. Chem.* **2019**, *8*, 496-505, doi:10.1002/ajoc.201900088.
43. Gichumbi, J.M.; Friedrich, H.B.; Omondi, B.; Naicker, K.; Singh, M.; Chenia, H.Y.J.J.o.C.C. Synthesis, characterization, antiproliferative, and antimicrobial activity of osmium (II) half-sandwich complexes. *J. Coord. Chem.* **2018**, *71*, 342-354.
44. Irgi, E.P.; Geromichalos, G.D.; Balala, S.; Kljun, J.; Kalogiannis, S.; Papadopoulos, A.; Turel, I.; Psomas, G.J.R.A. Cobalt (II) complexes with the quinolone antimicrobial drug oxolinic acid: structure and biological perspectives. *RSC Adv.* **2015**, *5*, 36353-36367.
45. Kouris, E.; Kalogiannis, S.; Perdih, F.; Turel, I.; Psomas, G. Cobalt(II) complexes of sparfloxacin: Characterization, structure, antimicrobial activity and interaction with DNA and albumins. *J. Inorg. Biochem.* **2016**, *163*, 18-27, doi:https://doi.org/10.1016/j.jinorgbio.2016.07.022.
46. Fiorini, V.; Zanoni, I.; Zacchini, S.; Costa, A.L.; Hochkoeppler, A.; Zanotti, V.; Ranieri, A.M.; Massi, M.; Stefan, A.; Stagni, S.J.D.T. Methylation of Ir (III)-tetrazolato complexes: An effective route to modulate the emission outputs and to switch to antimicrobial properties. *Dalton Trans.* **2017**, *46*, 12328-12338.
47. Chen, F.; Moat, J.; McFeely, D.; Clarkson, G.; Hands-Portman, I.J.; Furner-Pardoe, J.P.; Harrison, F.; Dowson, C.G.; Sadler, P.J. Biguanide Iridium(III) Complexes with Potent Antimicrobial Activity. *J. Med. Chem.* **2018**, *61*, 7330-7344, doi:10.1021/acs.jmedchem.8b00906.
48. Mendes, S.S.; Marques, J.; Mesterházy, E.; Straetener, J.; Arts, M.; Pissarro, T.; Reginold, J.; Berscheid, A.; Bornikoel, J.; Kluj, R.M., et al. Synergetic Antimicrobial Activity and Mechanism of Clotrimazole-Linked CO-Releasing Molecules. *ACS Bio & Med Chem Au* **2022**, 10.1021/acsbiomedchemau.2c00007, doi:10.1021/acsbiomedchemau.2c00007.
49. Sovari, S.N.; Radakovic, N.; Roch, P.; Crochet, A.; Pavic, A.; Zobi, F. Combatting AMR: A molecular approach to the discovery of potent and non-toxic rhenium complexes active against C. albicans-MRSA co-infection. *Eur. J. Med. Chem.* **2021**, *226*, 113858, doi:10.1016/j.ejmech.2021.113858.
50. Sovari, S.N.; Vojnovic, S.; Bogojevic, S.S.; Crochet, A.; Pavic, A.; Nikodinovic-Runic, J.; Zobi, F. Design, synthesis and in vivo evaluation of 3-arylcoumarin derivatives of rhenium(I) tricarbonyl complexes as potent antibacterial agents against methicillin-resistant Staphylococcus aureus (MRSA). *Eur. J. Med. Chem.* **2020**, *205*, 112533, doi:10.1016/j.ejmech.2020.112533.

51. Schindler, K.; Crochet, A.; Zobi, F. Aerobically stable and substitutionally labile α-diimine rhenium dicarbonyl complexes. *RSC Adv.* **2021**, *11*, 7511-7520, doi:10.1039/D1RA00514F.
52. Nasiri Sovari, S.; Kolly, I.; Schindler, K.; Cortat, Y.; Liu, S.C.; Crochet, A.; Pavic, A.; Zobi, F. Efficient Direct Nitrosylation of alpha-Diimine Rhenium Tricarbonyl Complexes to Structurally Nearly Identical Higher Charge Congeners Activable towards Photo-CO Release. *Molecules* **2021**, *26*, doi:10.3390/molecules26175302.
53. Kottelat, E.; Lucarini, F.; Crochet, A.; Ruggi, A.; Zobi, F. Correlation of MLCTs of Group 7 fac-[M(CO)(3)](+) Complexes (M = Mn, Re) with Bipyridine, Pyridinylpyrazine, Azopyridine, and Pyridin-2-ylmethanimine Type Ligands for Rational photoCORM Design. *Eur. J. Inorg. Chem.* **2019**, *2019*, 3758-3768, doi:10.1002/ejic.201900568.
54. Sovari, S.N.; Golding, T.M.; Mbaba, M.; Mohunlal, R.; Egan, T.J.; Smith, G.S.; Zobi, F. Rhenium(I) derivatives of aminoquinoline and imidazolopiperidine-based ligands: Synthesis, in vitro and in silico biological evaluation against Plasmodium falciparum. *J. Inorg. Biochem.* **2022**, *234*, 111905, doi:https://doi.org/10.1016/j.jinorgbio.2022.111905.
55. Delasoie, J.; Radakovic, N.; Pavic, A.; Zobi, F. Neovascularization Effects of Carbon Monoxide Releasing Drugs Chemisorbed on Coscinodiscus Diatoms Carriers Characterized by Spectromicroscopy Imaging. *Appl. Sci.* **2020**, *10*, doi:10.3390/app10207380.
56. Rossier, J.; Sovari, S.N.; Pavic, A.; Vojnovic, S.; Stringer, T.; Battig, S.; Smith, G.S.; Nikodinovic-Runic, J.; Zobi, F. Antiplasmodial Activity and In Vivo Bio-Distribution of Chloroquine Molecules Released with a 4-(4-Ethynylphenyl)-Triazole Moiety from Organometallo-Cobalamins. *Molecules* **2019**, *24*, doi:ARTN 231010.3390/molecules24122310.
57. Prieto, L.; Rossier, J.; Derszniak, K.; Dybas, J.; Oetterli, R.M.; Kottelat, E.; Chlopicki, S.; Zelder, F.; Zobi, F. Modified biovectors for the tuneable activation of anti-platelet carbon monoxide release. *Chem. Commun.* **2017**, *53*, 6840-6843, doi:10.1039/c7cc03642f.
58. Suliman, H.B.; Zobi, F.; Piantadosi, C.A. Heme Oxygenase-1/Carbon Monoxide System and Embryonic Stem Cell Differentiation and Maturation into Cardiomyocytes. *Antiox. Redox Sign.* **2016**, *24*, 345-360, doi:10.1089/ars.2015.6342.
59. Suliman, H.B.; Healy, Z.; Zobi, F.; Kraft, B.D.; Welty-Wolf, K.; Smith, J.; Barkauskas, C.; Piantadosi, C.A. Nuclear respiratory factor-1 negatively regulates TGF-β1 and attenuates pulmonary fibrosis. *iScience* **2022**, *25*, 103535, doi:https://doi.org/10.1016/j.isci.2021.103535.
60. Delasoie, J.; Schiel, P.; Vojnovic, S.; Nikodinovic-Runic, J.; Zobi, F. Photoactivatable Surface-Functionalized Diatom Microalgae for Colorectal Cancer Targeted Delivery and Enhanced Cytotoxicity of Anticancer Complexes. *Pharmaceutics* **2020**, *12*, 480.
61. Delasoie, J.; Pavic, A.; Voutier, N.; Vojnovic, S.; Crochet, A.; Nikodinovic-Runic, J.; Zobi, F. Identification of novel potent and non-toxic anticancer, anti-angiogenic and antimetastatic rhenium complexes against colorectal carcinoma. *Eur. J. Med. Chem.* **2020**, *204*, 112583, doi:https://doi.org/10.1016/j.ejmech.2020.112583.
62. Delasoie, J.; Rossier, J.; Haeni, L.; Rothen-Rutishauser, B.; Zobi, F. Slow-targeted release of a ruthenium anticancer agent from vitamin B-12 functionalized marine diatom microalgae. *Dalton Trans.* **2018**, *47*, 17221-17232, doi:10.1039/c8dt02914h.
63. Rossier, J.; Hauser, D.; Kottelat, E.; Rothen-Rutishauser, B.; Zobi, F. Organometallic cobalamin anticancer derivatives for targeted prodrug delivery via transcobalamin-mediated uptake. *Dalton Trans.* **2017**, *46*, 2159-2164, doi:10.1039/c6dt04443c.
64. Domenichini, A.; Casari, I.; Simpson, P.V.; Desai, N.M.; Chen, L.; Dustin, C.; Edmands, J.S.; van der Vliet, A.; Mohammadi, M.; Massi, M., et al. Rhenium N-heterocyclic carbene complexes block growth of aggressive cancers by inhibiting FGFR- and SRC-mediated signalling. *J. Exp. Clin. Cancer Res.* **2020**, *39*, 276, doi:10.1186/s13046-020-01777-7.
65. Collery, P.; Veena, V.; Harikrishnan, A.; Desmaele, D. The rhenium(I)-diselenoether anticancer drug targets ROS, TGF-β1, VEGF-A, and IGF-1 in an in vitro experimental model of triple-negative breast cancers. *Invest. New Drugs* **2019**, *37*, 973-983, doi:10.1007/s10637-019-00727-1.

66. Collery, P.; Santoni, F.; Ciccolini, J.; Tran, T.N.; Mohsen, A.; Desmaele, D. Dose Effect of Rhenium (I)-diselenoether as Anticancer Drug in Resistant Breast Tumor-bearing Mice After Repeated Administrations. *Anticancer Res.* **2016**, *36*, 6051-6057, doi:10.21873/anticanres.11194.
67. Collery, P.; Bastian, G.; Santoni, F.; Mohsen, A.; Wei, M.; Collery, T.; Tomas, A.; Desmaele, D.; D'Angelo, J. Uptake and efflux of rhenium in cells exposed to rhenium diseleno-ether and tissue distribution of rhenium and selenium after rhenium diseleno-ether treatment in mice. *Anticancer Res.* **2014**, *34*, 1679-1689.
68. Abram, U.; Hübener, R.; Alberto, R.; Schibli, R. Darstellung und Strukturen von (Et4N)2[Re(CO)3(NCS)3] und (Et4N)[Re(CO)2Br4]. *Z. anorg. allg. Chem.* **1996**, *622*, 813-818, doi:https://doi.org/10.1002/zaac.19966220511.
69. Santoro, G.; Beltrami, R.; Kottelat, E.; Blacque, O.; Bogdanova, A.Y.; Zobi, F. N-Nitrosamine-{cis-Re[CO](2))(2+) cobalamin conjugates as mixed CO/NO-releasing molecules. *Dalton Trans.* **2016**, *45*, 1504-1513, doi:10.1039/c5dt03402g.
70. Zobi, F.; Blacque, O.; Jacobs, R.A.; Schaub, M.C.; Bogdanova, A.Y. 17 e(-) rhenium dicarbonyl CO-releasing molecules on a cobalamin scaffold for biological application. *Dalton Trans.* **2012**, *41*, 370-378, doi:10.1039/c1dt10649j.
71. Carolus, H.; Van Dyck, K.; Van Dijck, P. Candida albicans and Staphylococcus Species: A Threatening Twosome. *Front. Microbiol.* **2019**, *10*, 2162, doi:10.3389/fmicb.2019.02162.
72. Mauri, A. alvaDesc: A Tool to Calculate and Analyze Molecular Descriptors and Fingerprints. 2020; pp. 801–820.
73. Lovering, A.L.; de Castro, L.H.; Lim, D.; Strynadka, N.C. Structural insight into the transglycosylation step of bacterial cell-wall biosynthesis. *Science* **2007**, *315*, 1402-1405, doi:10.1126/science.1136611.
74. Lovering, A.L.; Gretes, M.C.; Safadi, S.S.; Danel, F.; de Castro, L.; Page, M.G.; Strynadka, N.C. Structural insights into the anti-methicillin-resistant Staphylococcus aureus (MRSA) activity of ceftobiprole. *J. Biol. Chem.* **2012**, *287*, 32096-32102, doi:10.1074/jbc.M112.355644.
75. Yoshida, H.; Kawai, F.; Obayashi, E.; Akashi, S.; Roper, D.I.; Tame, J.R.; Park, S.Y. Crystal structures of penicillin-binding protein 3 (PBP3) from methicillin-resistant Staphylococcus aureus in the apo and cefotaxime-bound forms. *J. Mol. Biol.* **2012**, *423*, 351-364, doi:10.1016/j.jmb.2012.07.012.
76. Alexander, J.A.N.; Chatterjee, S.S.; Hamilton, S.M.; Eltis, L.D.; Chambers, H.F.; Strynadka, N.C.J. Structural and kinetic analyses of penicillin-binding protein 4 (PBP4)-mediated antibiotic resistance in Staphylococcus aureus. *J. Biol. Chem.* **2018**, *293*, 19854-19865, doi:10.1074/jbc.RA118.004952.
77. Lu, D.; Wormann, M.E.; Zhang, X.; Schneewind, O.; Grundling, A.; Freemont, P.S. Structure-based mechanism of lipoteichoic acid synthesis by Staphylococcus aureus LtaS. *Proc. Natl. Acad. Sci. USA* **2009**, *106*, 1584-1589, doi:10.1073/pnas.0809020106.
78. Ting, Y.T.; Harris, P.W.; Batot, G.; Brimble, M.A.; Baker, E.N.; Young, P.G. Peptide binding to a bacterial signal peptidase visualized by peptide tethering and carrier-driven crystallization. *IUCrJ* **2016**, *3*, 10-19, doi:10.1107/S2052252515019971.
79. Olatunji, S.; Yu, X.; Bailey, J.; Huang, C.Y.; Zapotoczna, M.; Bowen, K.; Remskar, M.; Muller, R.; Scanlan, E.M.; Geoghegan, J.A., et al. Structures of lipoprotein signal peptidase II from Staphylococcus aureus complexed with antibiotics globomycin and myxovirescin. *Nat. Commun.* **2020**, *11*, 140, doi:10.1038/s41467-019-13724-y.
80. Zhang, B.; Liu, X.; Lambert, E.; Mas, G.; Hiller, S.; Veening, J.W.; Perez, C. Structure of a proton-dependent lipid transporter involved in lipoteichoic acids biosynthesis. *Nat. Struct. Mol. Biol.* **2020**, *27*, 561-569, doi:10.1038/s41594-020-0425-5.
81. Percy, M.G.; Grundling, A. Lipoteichoic acid synthesis and function in gram-positive bacteria. *Annu. Rev. Microbiol.* **2014**, *68*, 81-100, doi:10.1146/annurev-micro-091213-112949.
82. Grundling, A.; Schneewind, O. Genes required for glycolipid synthesis and lipoteichoic acid anchoring in Staphylococcus aureus. *J. Bacteriol.* **2007**, *189*, 2521-2530, doi:10.1128/JB.01683-06.
83. Sham, L.T.; Butler, E.K.; Lebar, M.D.; Kahne, D.; Bernhardt, T.G.; Ruiz, N. Bacterial cell wall. MurJ is the flippase of lipid-linked precursors for peptidoglycan biogenesis. *Science* **2014**, *345*, 220-222, doi:10.1126/science.1254522.

84. Fishovitz, J.; Hermoso, J.A.; Chang, M.; Mobashery, S. Penicillin-binding protein 2a of methicillin-resistant Staphylococcus aureus. *IUBMB Life* **2014**, *66*, 572-577, doi:10.1002/iub.1289.
85. Richter, S.G.; Elli, D.; Kim, H.K.; Hendrickx, A.P.; Sorg, J.A.; Schneewind, O.; Missiakas, D. Small molecule inhibitor of lipoteichoic acid synthesis is an antibiotic for Gram-positive bacteria. *Proc. Natl. Acad. Sci. USA* **2013**, *110*, 3531-3536, doi:10.1073/pnas.1217337110.
86. Gründling, A.; Schneewind, O. Synthesis of glycerol phosphate lipoteichoic acid in Staphylococcus aureus. *Proc. Natl. Acad. Sci. USA* **2007**, *104*, 8478-8483, doi:doi:10.1073/pnas.0701821104.
87. Pasquina, L.W.; Santa Maria, J.P.; Walker, S. Teichoic acid biosynthesis as an antibiotic target. *Curr. Opin. Microbiol.* **2013**, *16*, 531-537, doi:10.1016/j.mib.2013.06.014.
88. Kuk, A.C.Y.; Hao, A.; Guan, Z.; Lee, S.-Y. Visualizing conformation transitions of the Lipid II flippase MurJ. *Nat. Commun.* **2019**, *10*, 1736, doi:10.1038/s41467-019-09658-0.
89. Kohga, H.; Mori, T.; Tanaka, Y.; Yoshikaie, K.; Taniguchi, K.; Fujimoto, K.; Fritz, L.; Schneider, T.; Tsukazaki, T. Crystal structure of the lipid flippase MurJ in a "squeezed" form distinct from its inward- and outward-facing forms. *Structure* **2022**, https://doi.org/10.1016/j.str.2022.05.008, doi:https://doi.org/10.1016/j.str.2022.05.008.
90. Sham, L.-T.; Butler, E.K.; Lebar, M.D.; Kahne, D.; Bernhardt, T.G.; Ruiz, N. MurJ is the flippase of lipid-linked precursors for peptidoglycan biogenesis. *Science* **2014**, *345*, 220-222, doi:doi:10.1126/science.1254522.
91. Craney, A.; Romesberg, F.E. The inhibition of type I bacterial signal peptidase: Biological consequences and therapeutic potential. *Bioorg. Med. Chem. Lett.* **2015**, *25*, 4761-4766, doi:10.1016/j.bmcl.2015.07.072.
92. Schmaler, M.; Jann, N.J.; Götz, F.; Landmann, R. Staphylococcal lipoproteins and their role in bacterial survival in mice. *Int. J. Med. Microbiol.* **2010**, *300*, 155-160, doi:https://doi.org/10.1016/j.ijmm.2009.08.018.
93. Vogeley, L.; Arnaout, T.E.; Bailey, J.; Stansfeld, P.J.; Boland, C.; Caffrey, M. Structural basis of lipoprotein signal peptidase II action and inhibition by the antibiotic globomycin. *Science* **2016**, *351*, 876-880, doi:doi:10.1126/science.aad3747.
94. Nguyen Minh, T.; Götz, F. Lipoproteins of Gram-Positive Bacteria: Key Players in the Immune Response and Virulence. *Microbiol. Mol. Biol. Rev. 80*, 891-903, doi:10.1128/MMBR.00028-16.
95. El Arnaout, T.; Soulimane, T. Targeting Lipoprotein Biogenesis: Considerations towards Antimicrobials. *Trends Biochem. Sci.* **2019**, *44*, 701-715, doi:https://doi.org/10.1016/j.tibs.2019.03.007.
96. Jendele, L.; Krivak, R.; Skoda, P.; Novotny, M.; Hoksza, D. PrankWeb: a web server for ligand binding site prediction and visualization. *Nucleic Acids Res.* **2019**, *47*, W345-W349, doi:10.1093/nar/gkz424 %J Nucleic Acids Research.
97. Wimley, W.C.; White, S.H. Experimentally determined hydrophobicity scale for proteins at membrane interfaces. *Nat. Struct. Mol. Biol.* **1996**, *3*, 842-848, doi:10.1038/nsb1096-842.
98. Zobi, F.; Kromer, L.; Spingler, B.; Alberto, R. Synthesis and Reactivity of the 17 e(-) Complex [(ReBr4)-Br-II(CO)(2)](2-): A Convenient Entry into Rhenium(II) Chemistry. *Inorg. Chem.* **2009**, *48*, 8965-8970, doi:10.1021/ic901031x.
99. Kurz, P.; Probst, B.; Spingler, B.; Alberto, R. Ligand Variations in [ReX(diimine)(CO)3] Complexes: Effects on Photocatalytic CO2 Reduction. *Eur. J. Inorg. Chem.* **2006**, *2006*, 2966-2974, doi:10.1002/ejic.200600166.
100. Murphy, B.L.; Marker, S.C.; Lambert, V.J.; Woods, J.J.; MacMillan, S.N.; Wilson, J.J. Synthesis, characterization, and biological properties of rhenium(I) tricarbonyl complexes bearing nitrogen-donor ligands. *J. Organomet. Chem.* **2020**, *907*, 121064, doi:https://doi.org/10.1016/j.jorganchem.2019.121064.
101. Chakraborty, I.; Jimenez, J.; Sameera, W.M.C.; Kato, M.; Mascharak, P.K. Luminescent Re(I) Carbonyl Complexes as Trackable PhotoCORMs for CO delivery to Cellular Targets. *Inorg. Chem.* **2017**, *56*, 2863-2873, doi:10.1021/acs.inorgchem.6b02999.
102. Sheldrick, G.M. Crystal structure refinement with SHELXL. *Acta Cryst. C* **2015**, *71*, 3-8.
103. Sheldrick, G.M. SHELXT - Integrated space-group and crystal-structure determination. *Acta Cryst. A* **2015**, *71*, 3-8.

104. Morris, G.M.; Huey, R.; Lindstrom, W.; Sanner, M.F.; Belew, R.K.; Goodsell, D.S.; Olson, A.J. AutoDock4 and AutoDockTools4: Automated docking with selective receptor flexibility. *J. Comput. Chem.* **2009**, *30*, 2785-2791, doi:10.1002/jcc.21256.

105. Chai, J.D.; Head-Gordon, M. Long-range corrected hybrid density functionals with damped atom-atom dispersion corrections. *Phys. Chem. Chem. Phys.* **2008**, *10*, 6615-6620, doi:10.1039/b810189b.

106. Chai, J.D.; Head-Gordon, M. Systematic optimization of long-range corrected hybrid density functionals. *J. Chem. Phys.* **2008**, *128*, 084106, doi:10.1063/1.2834918.

107. Grimme, S. Semiempirical GGA-type density functional constructed with a long-range dispersion correction. *J. Comput. Chem.* **2006**, *27*, 1787-1799, doi:10.1002/jcc.20495.

108. Becke, A.D. Density-functional thermochemistry. V. Systematic optimization of exchange-correlation functionals. *J. Chem. Phys.* **1997**, *107*, 8554-8560, doi:10.1063/1.475007.

109. Wu, Q.; Yang, W. Empirical correction to density functional theory for van der Waals interactions. *J. Chem. Phys.* **2002**, *116*, 515-524, doi:10.1063/1.1424928.

110. Andrae, D.; Häußermann, U.; Dolg, M.; Stoll, H.; Preuß, H. Energy-adjustedab initio pseudopotentials for the second and third row transition elements. *Theor.Chim. Acta* **1990**, *77*, 123-141, doi:10.1007/bf01114537.

111. Yan, C.; Yuan, R.; Pfalzgraff, W.C.; Nishida, J.; Wang, L.; Markland, T.E.; Fayer, M.D. Unraveling the dynamics and structure of functionalized self-assembled monolayers on gold using 2D IR spectroscopy and MD simulations. *Proc. Natl. Acad. Sci. USA* **2016**, *113*, 4929-4934, doi:10.1073/pnas.1603080113.

112. Vasighi, M.; Romanova, J.; Nedyalkova, M. A multilevel approach for screening natural compounds as an antiviral agent for COVID-19. *Comput. Biol. Chem.* **2022**, *98*, 107694, doi:10.1016/j.compbiolchem.2022.107694.